APPLIED SCIENCES AND ENGINEERING

O_2 variant chip to simulate site-specific skeletogenesis from hypoxic bone marrow

Hye-Seon Kim[1]†, Hyun-Su Ha[1]†, Dae-Hyun Kim[2], Deok Hyeon Son[1], Sewoom Baek[1], Jeongeun Park[1], Chan Hee Lee[1], Suji Park[1], Hyo-Jin Yoon[1], Seung Eun Yu[1], Jeon Il Kang[3], Kyung Min Park[3,4], Young Min Shin[1], Jung Bok Lee[5,6]*, Hak-Joon Sung[1]*

The stemness of bone marrow mesenchymal stem cells (BMSCs) is maintained by hypoxia. The oxygen level increases from vessel-free cartilage to hypoxic bone marrow and, furthermore, to vascularized bone, which might direct the chondrogenesis to osteogenesis and regenerate the skeletal system. Hence, oxygen was diffused from relatively low to high levels throughout a three-dimensional chip. When we cultured BMSCs in the chip and implanted them into the rabbit defect models of low-oxygen cartilage and high-oxygen calvaria bone, (i) the low oxygen level (base) promoted stemness and chondrogenesis of BMSCs with robust antioxidative potential; (ii) the middle level (two times ≥ low) pushed BMSCs to quiescence; and (iii) the high level (four times ≥ low) promoted osteogenesis by disturbing the redox balance and stemness. Last, endochondral or intramembranous osteogenesis upon transition from low to high oxygen in vivo suggests a developmental mechanism–driven solution to promote chondrogenesis to osteogenesis in the skeletal system by regulating the oxygen environment.

INTRODUCTION

O_2 regulates cell differentiation and the consequent multiorganogenesis. The O_2 level varies throughout the organ and tissue types as well as from the embryo to the adult body. In contrast to the 21% O_2 level in the ambient environment, 2 to 10% is maintained in the body because O_2 passes through the lung and then the vascular circulatory system to reach each organ in smaller amounts. As a result, vascular transport distributes O_2 to multiple organs in a gradient fashion, with outside-in diffusion into organs and tissues. In the skeletal system, O_2 diffuses through neighboring tissues to maintain 5 to 10% in the vascularized bone, 2 to 7% in the hypoxic bone marrow, and 1 to 5% in the nonvascularized cartilage (1). Hypoxic bone marrow serves as a production site and reservoir of bone marrow mesenchymal stem cells (BMSCs) with high stemness and proangiogenic potential (2). Hence, the formation of the vascularized bone and vessel-free cartilage (osteochondrogenesis) from the bone marrow might be critically regulated by the organ-specific O_2 levels and consequent BMSC actions representing a punchline value to reveal an unidentified role of the most common environmental factor in the development and regeneration of multiple organs.

Studies have reported that O_2 levels regulate cellular energy production, metabolism (3), proliferation, and differentiation (4–6).

Therefore, the diffusive variation in O_2 levels throughout multiple organs appears to play regulatory roles in the collaborative functions of neighboring organs. As a key signaling mechanism to program these roles, abnormal O_2 levels induce expression, stabilization, and degradation of hypoxia-inducible factor 1α (HIF1-α) (7) in association with the signaling actions of reactive oxygen species (ROS) (8). As a result of high ROS production, oxidative stress and cell aging (9) can be progressed upon insufficient activation of the antioxidant defense system. These mechanistic actions vary depending on cell type, tissue function, disease status, and organ environment.

However, BMSCs undergo chondrogenic differentiation in the vessel-free cartilage with environment-responsive changes in stem cell characteristics and proliferation (6). Hence, a vessel-free hypoxic environment most likely plays a key role in healthy cartilage regeneration. As mechanistic actions control the chondrogenesis of BMSCs, (i) stabilization of HIF1-α promotes chondrogenic metabolism by inducing cell aggregation; (ii) HIF1-α also increases the expression of sex-determining region Y-box 9 (SOX9) and the consequent transcription of type II collagen (10) by inhibiting osteogenesis and suppressing type 1 collagen production (1, 11–13); and (iii) as the proangiogenic potential of BMSCs increases under hypoxic conditions, the expression of vascular endothelial growth factor (VEGF) is promoted in the cartilage to maintain homeostasis and proliferation of chondrocytes. However, VEGF function is deactivated by antiangiogenic factors (e.g., chondromodulin1 and tenomodulin) during chondrogenic maturation (14, 15). Although the same hypoxic environment with the bone marrow, the operation of these mechanisms promotes vessel-free chondrogenesis of BMSCs.

Vascularization of bone tissues establishes a relatively high-O_2 environment through outside-in diffusion and circulatory delivery compared to the hypoxic bone marrow and vessel-free cartilage. Two pro-osteogenic mechanisms can be suggested: (i) During endochondral osteogenesis, the hypoxic bone marrow–preserved stemness of BMSCs is used for chondrogenesis in the

[1]Department of Medical Engineering, Graduate School of Medical Science, Brain Korea 21 Project, Yonsei University College of Medicine, Seoul 03722, Republic of Korea. [2]Department of Veterinary Surgery, College of Veterinary Medicine, Chungnam National University, Daejeon 34134, Republic of Korea. [3]Department of Bioengineering and Nano-Bioengineering, College of Life sciences and Bioengineering, Incheon National University, Incheon 22012, Republic of Korea. [4]Research Center for Biomaterials and Process Development, Incheon National University, Incheon 22012, Republic of Korea. [5]Department of Biological Sciences, Sookmyung Women's University, Seoul 04310, Republic of Korea. [6]Research Institute of Women's Health, Sookmyung Women's University, Seoul 04310, Republic of Korea.
†These authors contributed equally to this work.
*Corresponding author. Email: hj72sung@yuhs.ac (H.-J.S.); jungboklee@sookmyung.ac.kr (J.B.L)

nonvascularized environment. Next, chondrocytes become hypertrophic via the expression of VEGF, matrix metalloproteinase 13 (MMP13), and runt-related transcription factor 2 (RUNX2) (16–19), thereby promoting osteogenesis within a type I collagen (COL1)–rich environment. (ii) During intramembranous osteogenesis, the bone is formed by the direct differentiation of BMSCs into osteoblasts via the expression of VEGF and RUNX2 (20). O_2 supply in the vascularized bone might contribute to osteogenic processes because of the stabilization of HIF1-α with high ROS production (10, 21–23). Hence, the diffusive variation in O_2 levels throughout the bone marrow, cartilage, and bone indicates a supportive potential to guide osteochondrogenesis.

Among the various types of cells in the bone marrow, we used BMSCs in this study because they are produced in the bone marrow and proven to differentiate from osteochondrogenic cells in a wide range of studies. Moreover, this cell type is known to have the O_2 effect–regulated properties, including maintenance of the healthy naïve phenotype with the proangiogenic potential in the hypoxia-like bone marrow (2) and potent resistance to O_2 level variation–derived oxidative stress by scavenging ROS (24, 25). We modeled the variation in the O_2 level in the skeletal system in a chip, where BMSCs could be cultured in a three-dimensional (3D) gel. Because two channels passed through the chip, the culture media were perfused to enable O_2 diffusion into the area between the channels, and excessive O_2 was generated into one of the channels through the catalase reaction with H_2O_2. In this way, high, middle, and low O_2 level areas were set up in the chip through diffusive variation of the media from the two channels. We matched the three O_2 levels with the measured O_2 levels in the vascularized bone area, hypoxic bone marrow, and vessel-free cartilage of the rat bone after harvesting and confirmed them by computational modeling. In rabbits, defects of the femur cartilage and calvaria served as regeneration models with vessel-free low-O_2 and vascularized environments, respectively. As seen in the transition from the bone marrow to cartilage, the low-O_2 environment promoted proangiogenic stemness with robust antioxidative potential to vessel-free chondrogenesis of BMSCs upon support by prochondrogenic factors. The middle level pushed BMSCs to undergo the quiescence stage with the least proliferative characteristics. The high O_2 level disturbed the redox balance and stemness with high oxidative stress, thereby promoting bone formation upon pro-osteogenic stimulation. We observed chondrogenesis to osteogenesis upon transition from low to high O_2 levels at the boundary between the vessel-free cartilage and vascularized bone in the femur defect. This study identified the supportive roles of the most common physiological factor (O_2) in osteochondral regeneration using a unique chip technology to overcome prior experimental limits.

RESULTS

Fabrication and characterization of O_2 variant chip

In a real physiological model using rats, a needle-type O_2 microsensor recorded the O_2 levels (%) in the vessel-free cartilage, vascularized bone, and hypoxic bone marrow to average 1.2, 8.7, and 6%, respectively (Fig. 1A). We modeled these three O_2 levels using an O_2 variant chip after production with the following production process (fig. S2). (i) We equipped the polydimethylsiloxane (PDMS) mold with two parallel capillary tubes for medium perfusion . (ii) We poured a gelatin/microbial transglutaminase (mTG) solution in a mixture of BMSCs into the mold, followed by mTG cross-linking at 37ºC for 10 min to maintain the structure stability of gelatin so that channels can be produced without rupturing. (iii) When we perfused each channel with culture media using a peristaltic pump, O_2 was produced in one of the channels with medium circulation. Catalase was embedded in gelatin hydrogel and reacted with H_2O_2 within a tube reservoir for perfusion using a syringe pump.

Then, we applied computational fluid dynamics (CFD) modeling to confirm the three site-specific variations in O_2 levels through the simulation of O_2 diffusion and consumption (Fig. 1, B and C). We set the in-chip oxygen outflow to $1.15 \times 10^{-12}\,\mathrm{kg\,s^{-1}}$ in the computational modeling by considering the oxygen consumption of BMSCs (see Supplementary Text). The results validated the feasibility of computer simulation in matching with the physiological O_2 levels at the relative change from the low (base) to the middle (two times ≥ low) and further to the high (four times ≥ low) levels rather than the absolute values. Color coding from contour and volume rendering via 3D modeling showed the O_2 levels, followed by quantitative determination [Red: High O_2 area (media + O_2 generation); Green: Middle O_2 area (media only); and Blue: Low O_2 area]. Perfusing safranin-O (red, high) and crystal violet (violet, middle) showed the diffusive color gradient as an indication of the O_2% variation in two channels separately for 72 hours (Fig. 1D and fig. S3). Although the holes were generated by punching to embed the gelatin hydrogel with cells into the chip, the holes did not affect the gradient generation because the readout concentrations of O_2 were aligned with the results of the computer simulation. These results validated the utility of the chip to model the diffusive variation of O_2 levels, as seen in the hypoxic bone marrow, vessel-free cartilage, and vascularized bone.

Because BMSCs need to be 3D cultured on the chip under O_2 generation, we determined the concentrations of H_2O_2, gelatin, and catalase (fig. S4). H_2O_2 reacted with catalase to generate O_2 in the gelatin gel for 3 days, and, consequently, we determined the maximum H_2O_2 concentration to be 100 μM (fig. S4A). This was the maximum concentration to maintain BMSC viability on day 1 (>90%) and day 3 (>50%) by considering complete H_2O_2 consumption through the reaction within 1 day. We determined the gelatin concentration to be 10% (w/v) because we did not observe any gel flow, in contrast to 5% (w/v) in the inverted vial (fig. S4B). Catalase reacted with 100 μM H_2O_2 with mTG cross-linking for 3 days. Because an enzymatic reaction might promote gel degradation and result in a culture instability, we determined the maximum catalase concentration to be 5 mg by checking out less than 10% degradation on day 1 with no notable difference from that of 10 mg on day 3 (fig. S4C). We generated O_2 in the media by reacting catalase with H_2O_2 for 30 min until saturation, as determined with an oxygen microsensor (Fig. 1E). When the O_2 concentration increases, the ruthenium signal decreases by quenching the O_2 (26). After generating O_2 in the left channel for 0 and 72 hours in the triple chip replicates, we validated the area-dependent variation of the O_2 level as the ruthenium signal increased from the high- to middle-O_2 area and further to the low-O_2 area (Fig. 1F and fig. S5) in the chip under medium perfusion into both channels. The O_2 levels were double confirmed by the oxygen sensor in the same setting of the chip (Fig. 1G). The O_2 concentrations of three areas from the ruthenium signals and oxygen sensor were aligned with the results of the computational simulation.
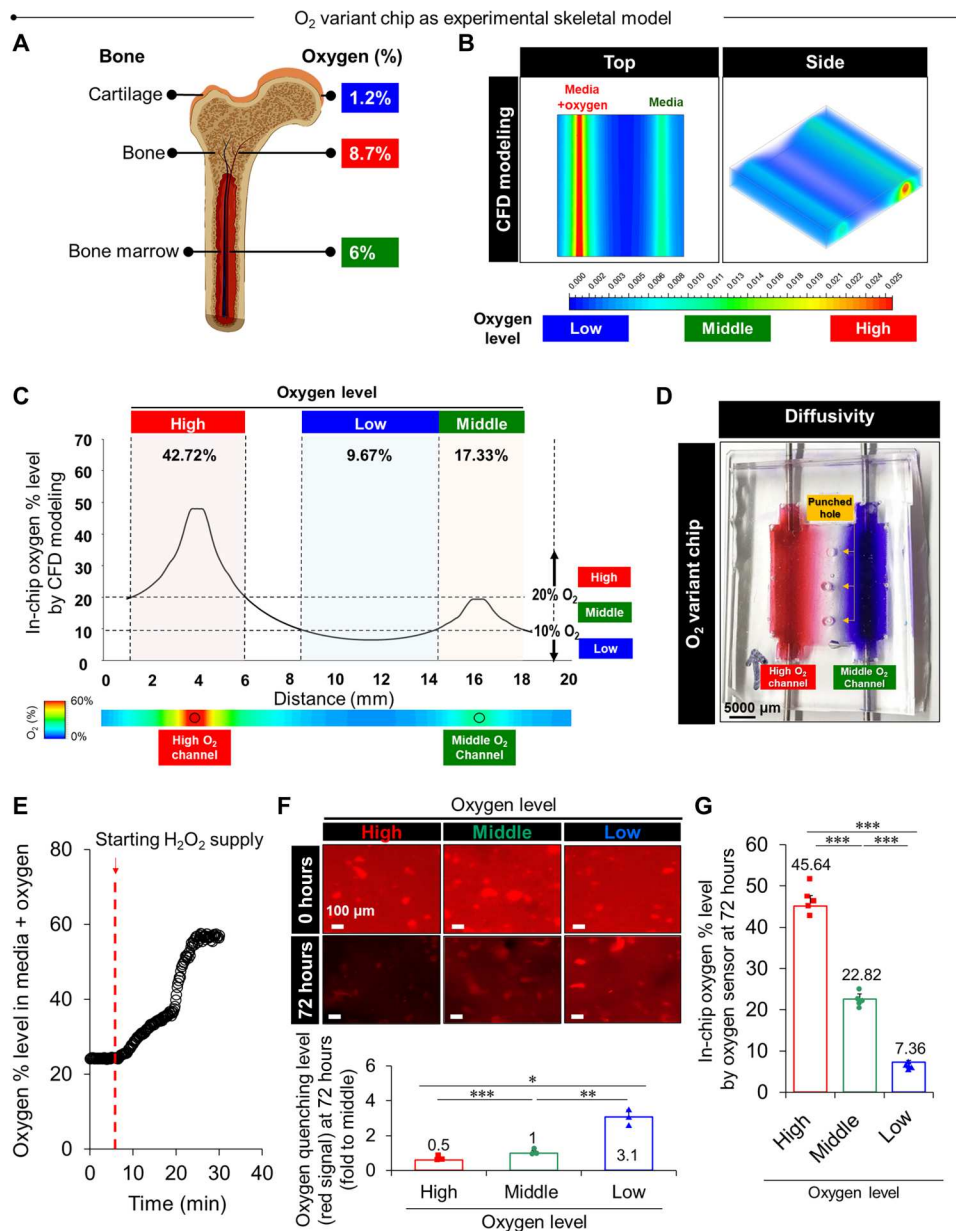
Fig. 1. Characterization of area-dependent O_2 levels in the chip as an experimental skeletal model. (**A**) We measured the O_2 levels (%) in the cartilage, bone, and bone marrow of rats using a needle-type O_2 microsensor. (**B**) To simulate the bone site–specific variations of O_2 levels in the chip, we used CFD modeling of O_2 diffusion and consumption, as shown by the color coding from contour and volume rendering via 3D modeling, followed by (**C**) quantitative determination [red media + O_2 generation (high), green media only (middle), and blue (low)]. (**D**) To show the diffusive color gradient as an indication of the O_2% variations, we perfused safranin-O (red, high) and crystal violet (violet, middle) in two channels separately for 6 hours (yellow, punched holes to embed hydrogel and cells). (**E**) O_2 was generated into media by reacting catalase with H_2O_2 until saturation for 30 min as determined using an oxygen microsensor. (**F**) After generating O_2 in the left channel for 0 and 72 hours, we determined the area-dependent oxygen levels in the chip under medium perfusion into both channels through oxygen quenching by ruthenium whose red fluorescence intensity decreased upon incremental oxygen levels (top) with quantitative analysis (bottom) ($n = 3$). (**G**) The area-dependent oxygen levels were determined by the oxygen sensor after O_2 generation in the left channel for 72 hours ($n = 5$). Data = means ± SD. *$P < 0.05$, **$P < 0.01$, and ***$P < 0.001$ between the lined groups.

Hence, we set up culture conditions to expose BMSCs to high, middle, and low O_2 levels in a 3D gel perfusion system. The three areas were defined by considering that cells recognize gradient changes in the same space (27, 28). The O_2 level increased from the cartilage to bone marrow more than twice and to the bone more than four times. The computer simulation results exhibited the same steps of increase in the O_2 level from 0 to 10% (low) to

10 to 20% (middle) and an average of 42.7% (high) in alignment with the measurement results using ruthenium and oxygen sensor. Together, the three areas were separated by the low (base), middle (two times ≥ low), and high (four times ≥ low) levels of O_2. As a validation of cellular response to the O_2 gradient in the chip, the O_2 level–guided migration of chondrocyte versus osteoblast was examined over time for 72 hours (fig. S6). Human chondrocytes

migrated gradually further toward the low-O_2 area from both the high- and middle-O_2 areas over time. In contrast, mouse osteoblasts (MC3T3) migrated to the high-O_2 area from the low-O_2 area following the incremental gradient of the O_2 level, but the middle-O_2 area did not exhibit any migration pattern due to the decremental O_2 level toward the neighboring low-O_2 area. The results indicate the low- and high-O_2 nature of chondrogenic and osteogenic environments, respectively.

Stemness of BMSCs in O_2 variant chip

Because O_2 diffused throughout the chip, we first confirmed intact BMSC viability in the three areas on day 3 after culture (fig. S7, A and B). In alignment with the hypoxic environment of the bone marrow, the low-O_2 area promoted BMSC stemness the most among the three areas, as determined by marker expression of the gene [sex determining region Y-box transcription factor 2 (SOX2), octamer-binding transcription factor 4 (OCT4), nanog homeobox (NANOG), and growth differentiation factor 3 (GDF3)] and protein (SOX2 and OCT4) levels (Fig. 2, A and B). The expression of BMSC marker genes (CD90, CD105, and CD73) was also promoted in the low- and high-O_2 areas compared to the middle-O_2 area (Fig. 2C).

We noticed the prostemness effect of the low-O_2 area by most proangiogenic characteristics of BMSCs as determined by marker expression at the gene [CD34, platelet endothelial cell adhesion molecule 1 (PECAM1), vascular endothelial growth factor receptor 2 (Flk1), Flk1, vascular endothelial growth factor (VEGF), and Angiopoietin 1 (ANGPT1), and platelet-derived growth factor receptor β (PDGFRβ)] levels (Fig. 2D) compared to the high- and middle-O_2 areas. The results were supported by the overall trend indicating that the expression of proangiogenic protein markers increased from the middle- to the high-O_2 area and further to the low-O_2 area (Fig. 2E and fig. S8). First, as an indication of stemness maintenance, the proteins representing the early angiogenic potential were expressed most distinctively in the low-O_2 area compared to the other areas. In particular, the most expression of granulocyte-macrophage colony-stimulating factor (GM-CSF) in the low-O_2 area represents the potential to promote hematopoiesis in the bone marrow (*29*) and to trigger a chondrogenic foundation (*30*) in addition to angiogenic stimulation, which was attenuated in the high-O_2 area. Next, the signature of extracellular matrix (ECM) remodeling was seen in both low- and high-O_2 areas for chondrogenesis and osteogenesis, respectively, as evidenced by the expression of MMPs. Last, while the process such as endothelial cell (EC)–to–MSC transition likely supported the appearance of angiogenic signatures in both areas (*31–33*), the relatively more expression of tumor necrosis factor–α (TNF-α) in the high-O_2 area indicates the supportive roles in MSC proliferation and osteogenic differentiation (*34–38*).

Consequently, BMSCs in the low-O_2 area exhibited the highest self-renewal potential of BMSCs as determined by marker gene expression [Cyclin A (CCNA) and Cyclin B (CCNB), Cyclin-dependent kinase 1 (CDK1), and cyclin-dependent kinase 2 (CDK2)] with maintenance of the highest energy [adenosine 5′-triphosphate (ATP)] level (Fig. 2, F and G). BMSCs were produced with high stemness (i.e., self-renewal and differentiation potentials) in the bone marrow under the low-O_2 condition (2 to 7%) compared to the ambient level (21%) (*39*, *40*). Hence, these results suggest the need for a low O_2 level to preserve BMSC stemness, as seen in the hypoxic bone marrow, similar to the birthplace effect. Moreover,

the stemness of BMSCs under the high-O_2 condition was higher than that of the middle-O_2 condition. The high-O_2 condition appeared to make BMSCs ready for osteogenic differentiation by increasing the stemness and angiogenic potential with a reduction of both cell cycle activity and energy. Stem cells use the energy for either self-renewal or differentiation rather than carrying out both activities simultaneously (*41–43*).

Redox balance and growth control of BMSCs in O_2 variant chip

High or low O_2 levels induce the expression and degradation of HIF1-α (*7*) upon collaborative regulation by ROS (*8*), resulting in a redox balance. After culturing in the chip for 3 days, both high- and low-O_2 areas exhibited higher HIF1-α expression in BMSCs than in the middle-O_2 area (Fig. 3A). However, only the low-O_2 area helped BMSCs maintain antioxidative enzyme activities with higher expression of antioxidative genes [glutathione S-transferase alpha 2 (GSTA2), superoxide dismutase 2 (SOD2), and thioredoxin-1 (TXN)], indicating regulation of the redox balance (Fig. 3, B and C). In contrast, the high- and middle-O_2 areas induced oxidative stress in BMSCs, as evidenced by a higher NADH [reduced form of nicotinamide adenine dinucleotide (NAD$^+$)]/NAD$^+$ ratio and increased fluorescence signals of ROS, thereby disturbing the redox balance (Fig. 3, D and E). Hence, the high and middle O_2 levels induced HIF1-α–related and independent oxidative stress in BMSCs, respectively.

This disturbed redox balance increased BMSC growth in the high-O_2 area, in contrast to the quiescent growth seen in the middle-O_2 area, as evidenced by proliferation marker expression at the gene [Ki67, proliferating cell nuclear antigen (PCNA), extracellular signal–regulated kinase (ERK), and AKT] and protein (ERK and AKT) levels (Fig. 3, F and G). The gene expression of cell cycle indicators (CCNC, CCND, CDK3, and CDK4) further supported our results (Fig. 3H). The high-O_2 area induced BMSCs to move from G_0 to G_1, the most among the test groups, and thereby reaching G_1 at the level seen in the low-O_2 area, in contrast to the shutdown of cell cycle progression in the middle-O_2 area. The maintenance of the redox balance by low O_2 resulted in the control of BMSC growth. Abnormally proliferative BMSCs under high-O_2 conditions expressed more anti–self-renewal genes (p16 and p21) compared to the other areas, indicating differentiation into a specific lineage for regeneration (Fig. 3I). These results suggest a key role for bone marrow hypoxia in maintaining the redox balance and self-renewal capability of BMSCs. Upon transition from hypoxia to the vascularized bone, the high-O_2 condition promoted the regenerative proliferation of BMSCs by disturbing the redox balance.

Chondro-to-osteogenesis of BMSCs upon transition of O_2 level

After 3 days of culture on the chip, we exposed BMSC to chondrogenic induction media for 14 days under the general normoxia (20% O_2) condition. In this way, the 3-day chip culture was used to set the O_2 level–dependent potential of BMSCs for the next 14-day differentiation regardless of the O_2 variation situations, such as development, damage, regeneration, and pathogenesis in cartilages. The media served an environmentally inductive role in cartilage regeneration, as seen in vivo so that we could investigate the effect of the area-dependent O_2 level on chondrocyte differentiation of BMSC.
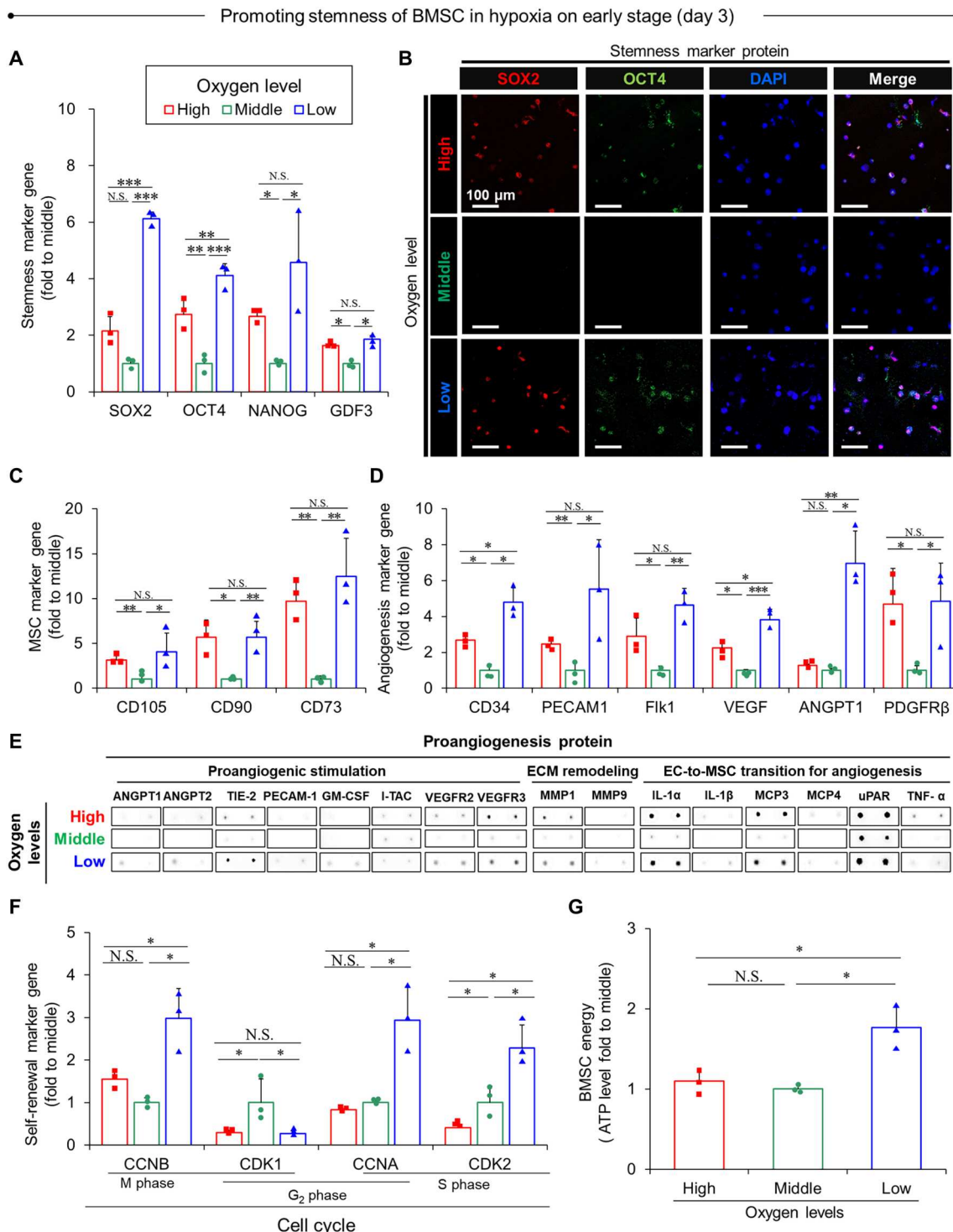
Fig. 2. Hypoxia in O₂ variant chip as a key factor to promote stemness of BMSC. When we cultured BMSCs in the O₂ variant chip for 3 days, the hypoxic low-O₂ area promoted BMSC stemness the most among the three areas as determined by marker expression of (**A**) gene (SOX2, OCT4, NANOG, and GDF3) and (**B**) protein (SOX2 and OCT4) levels in alignment with (**C**) BMSC marker genes (CD90, CD73, and CD105). The prostemness effect of low-O₂ area was evidenced further by most proangiogenic characteristics of BMSCs, as determined by most expression at (**D**) gene markers [CD34, platelet endothelial cell adhesion molecule 1 (PECAM1), Flk1, VEGF, ANGPT1, and platelet-derived growth factor receptor β (PDGFRβ)] with (**E**) protein blot signals covering all selected proangiogenic makers compared to the high- and middle-O₂ areas. Consequently, BMSCs in the low-O₂ area exhibited (**F**) the most superior self-renewal potential of BMSCs as determined by marker gene expression (CCNA, CCDB, CDK1, and CDK2) with (**G**) maintenance of the highest energy [adenosine 5′-triphosphate (ATP)] level. Data = means ± SD. *$P < 0.05$, **$P < 0.01$, and ***$P < 0.001$ between the lined groups. ($n = 3$ for all experiments). N.S., not significant; DAPI, 4′,6-diamidino-2-phenylindole; IL-1α, interleukin-1α;IL-1β, interleukin-1β; TIE-2, Tyrosine-protein kinase receptor; I-TAC, Interferon-inducible T-cell alpha chemoattractant; MCP3, Monocyte chemotactic protein-3; uPAR, Urokinase-type plasminogen activator receptor.
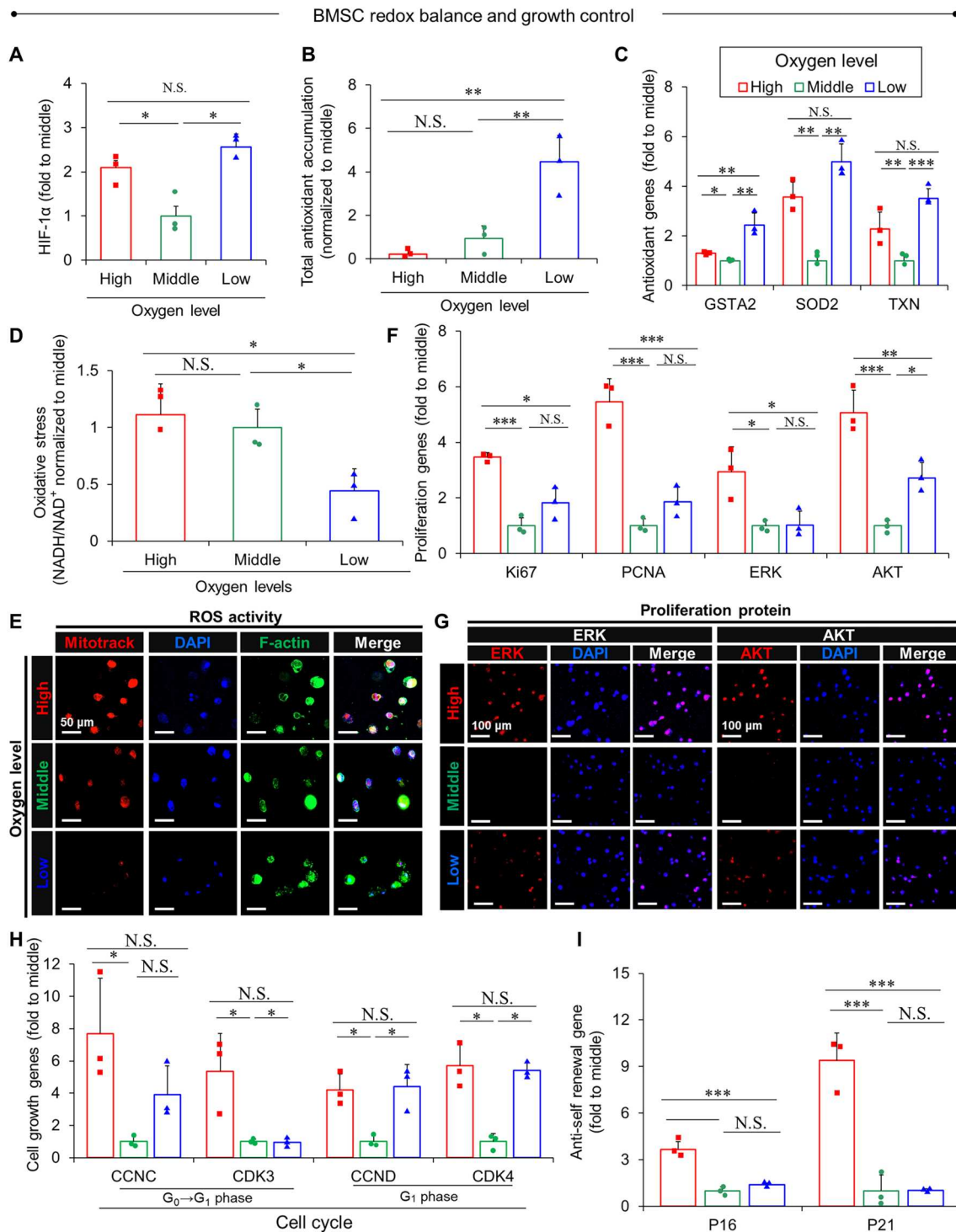
Fig. 3. Hypoxia-mediated maintenance of BMSC redox balance and growth control in the chip. When we cultured BMSCs in the chip for 3 days, (**A**) both high- and low-O$_2$ areas exhibited higher HIF-1-α expression compared to the middle-O$_2$ area. However, only the low-O$_2$ area helped BMSCs maintain (**B**) the most antioxidative activities with (**C**) higher expression of supportive genes (GSTA2, SOD2, and TXN), compared to the other areas. As a result, the high- and middle-O$_2$ areas induced oxidative stress in BMSCs as evidenced by (**D**) a higher NADH/NAD$^+$ ratio and (**E**) more fluorescence signals of ROS in contrast to the hypoxic area. Hence, the high- and middle-O$_2$ areas induced HIF1-α–related and independent oxidative stress in BMSCs, respectively. We noticed abnormal increases in BMSC growth in the high-O$_2$ area in contrast to the growth quiescence in the middle-O$_2$ area, as evidenced by marker expression at (**F**) gene [Ki67, proliferating cell nuclear antigen (PCNA), extracellular signal–regulated kinase (ERK), and AKT] and (**G**) protein (ERK and AKT) levels compared to the hypoxic area. These results were further supported by (**H**) gene expression of cell cycle indicators (CCNC, CCND, CDK3, and CDK4). The maintenance of redox balance by low O$_2$ resulted in control of BMSC growth. (**I**) Abnormally proliferative BMSCs under high O$_2$ expressed more anti–self-renewal genes (p16 and p21) compared to the other areas. Data = means ± SD. *$P < 0.05$, **$P < 0.01$, and ***$P < 0.001$ between the lined groups. ($n = 3$ for all experiments).

The low-O_2 area promoted the expression of chondrogenic markers [SOX9, aggrecan, and collagen type II alpha 1 chain (Col2a1)] and protein levels (aggrecan and Col2a1) (Fig. 4, A and B). The results were confirmed by the increased production of glycosaminoglycan (GAG) in the low-O_2 area compared to the high- and middle-O_2 area (fig. S9), indicating a causative role of the hypoxic O_2 environment in promoting the chondrogenic action. The O_2 variation was modeled; however, other environmental factors of the cartilage and bone in the induction media could not be supplied to each area separately in the chip. The three levels of O_2 level variation among the cartilage, bone marrow, and bone were measured using an oxygen sensor (Fig. 1A), indicating the natural formation of the O_2 level gradient from the vascularized bone to the vessel-free cartilage. The generation of defect left room for sample implantation, and

Fig. 4. Chondro-to-osteogenesis of BMSCs upon transition from low- to high-oxygen environment. (**A** and **B**) We treated BMSCs with chondrogenic induction media after culture in an O_2 variant chip for 3 days and determined their chondrogenesis according to oxygen levels in vitro. The low O_2–mediated chondrogenesis was evidenced by (A) the gene expression of chondrogenic differentiation–related markers (SOX9, aggrecan, and Col2a1) and (B) the immunostaining of aggrecan (green) and Col2a1 (red) on days 7 and 14 (*n* = 3). (**C** and **E** to **H**) chondrogenesis to osteogenesis of BMSCs upon transition from low- to high-oxygen environment was determined using a rabbit cartilage defect model in vivo following (C) the experimental procedure (*n* = 5). (**D**) In a mouse, perfusion staining with microbeads showed the absence and presence of blood vessels in the low-O_2 cartilage (dashed line) and high-O_2 bone (solid line) in the low (left, 2.5×) and high (right, 10×) magnifications. (E) First, at the vessel-free low-O_2 area, BMSCs underwent chondrogenesis exclusively as observed by the safranin-O staining (yellow line, defect area for sample implantation) after sample implantation for 4 weeks. This result was further evidenced by (F) protein expression of chondrogenic-related markers (i) SOX9, (ii) aggrecan, and (iii) Col2a1 with HuNu. (G) Next, at the subchondral bone near vasculature, osteogenesis because of hypertrophic chondrocyte differentiation of BMSCs in response to the increased O_2 level was exhibited by μ-CT images (left, dashed yellow line, defect area for sample implantation) with quantitative analysis (right) of new bone volume. (H) Immunostaining of hypertrophic chondrocyte–related markers (i) MMP9, (ii) MMP13, and (iii) ColX with staining of HuNu toward osteogenesis. Data = means ± SD. *$P < 0.05$, **$P < 0.01$, and ***$P < 0.001$ between the lined groups.
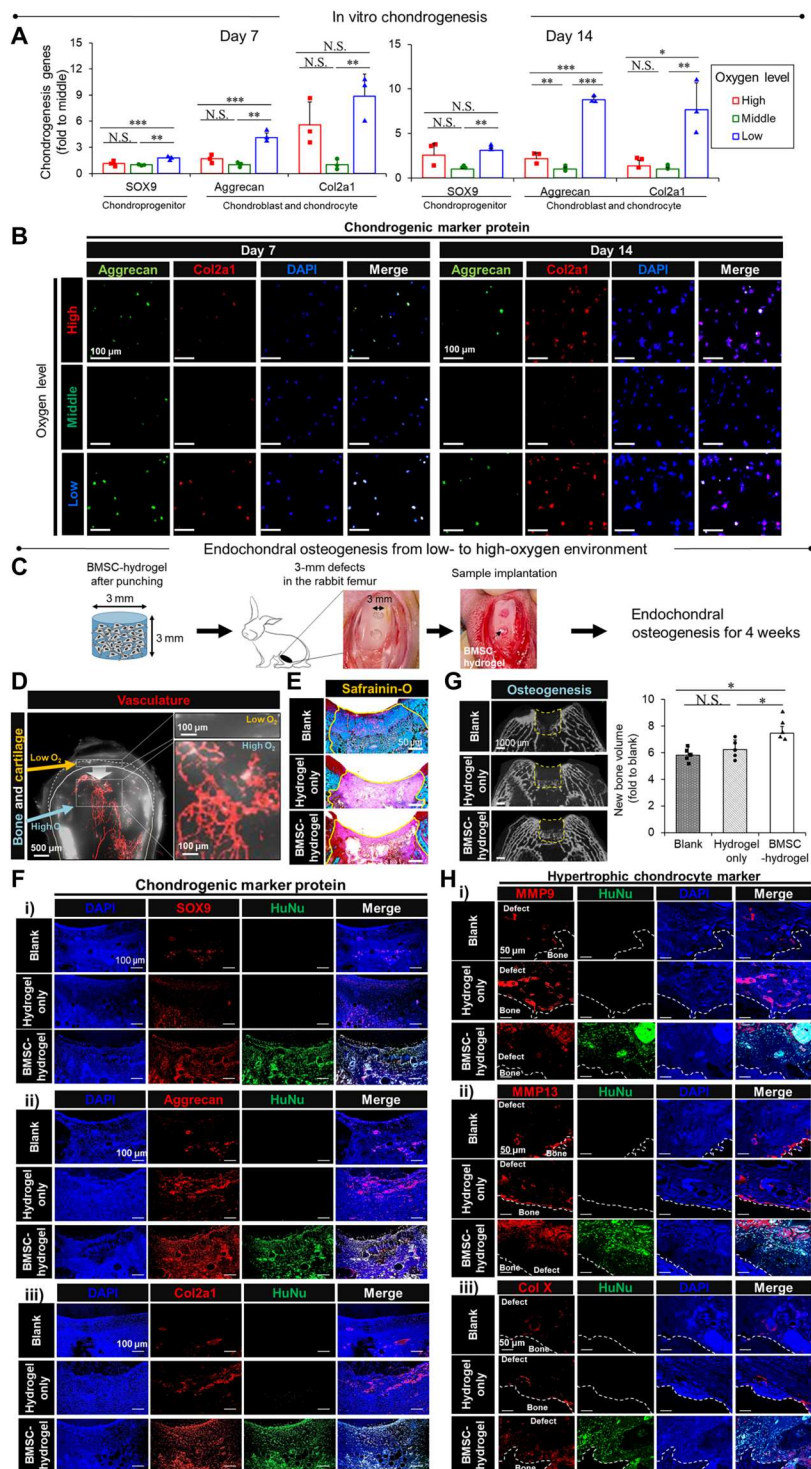
the use of hydrogel for BMSC embedding prevented direct influences of tissue interaction with BMSCs to maximize the effect of diffusible gasses such as O_2. Hence, we used a defect model of rabbit articular cartilage to transplant BMSCs with a hydrogel so that the implant could interact with both the vessel-free cartilage and vascularized bone sides simultaneously as an in vivo model to mimic the O_2 gradient of the chip (Fig. 4C). In this way, the relationship of O_2 level with chondrogenesis or osteogenesis was examined. Therefore, after BMSCs were embedded in a fresh gelatin hydrogel without prior culture in the chip, we immediately implanted the test samples (blank, only hydrogel, and BMSC-hydrogel).

When we perfused mice with microbeads to stain the vasculature in the entire body before the defect with sample implantation, we noticed the absence of vessels in the normal cartilage, in contrast to the normal vascularized bone (Fig. 4D). These conditions naturally set up low and high O_2 levels with complete support from two naturally generated environments. When an osteochondral defect was generated, the sides of vessel-free cartilage and vascularized bone are presented separately around the defect, resulting in clear differences in O_2 level between the bone and cartilage sides. The chondrogenic effects in the vessel-free areas of sample implantation were incremental from blank to hydrogel only and much further to BMSC-hydrogel, as shown by safranin-O staining (Fig. 4E) and the expression of protein markers (SOX9, aggrecan, and Col2a1) with staining of human nuclei (HuNu) (Fig. 4F). These results indicate a synergistic action between the hydrogel and BMSCs in promoting cartilage regeneration, and the hypoxic environment supported this action toward chondrogenesis rather than osteogenesis. In contrast, each vascularized side served as a sprouting point of new bone generation toward the defect side, and this osteogenesis effect was also incremental from blank to hydrogel only and, more significantly, to BMSC-hydrogel. The supporting results include micro–computed tomography (µ-CT) imaging with quantitative analysis of new bone volume (Fig. 4G) and protein marker expression of hypertrophic chondrocytes (MMP13, MMP9, and ColX) as a phenotypic indication of transformation toward osteogenesis (Fig. 4H) (*19*, *38*, *44*, *45*). This process was likely supported by a process like endochondral osteogenesis because the vessel-free cartilage in the hypoxic areas was gradually filled by the bone sprouting from the existing bone sides upon O_2 supply through the vasculature.

Osteogenesis of BMSCs by high O_2 level
After 3 days of culture on the chip, we exposed BMSC to osteogenic induction media for 14 days under the general normoxia (20% O_2) condition. In this way, the 3-day chip culture was used to set the O_2 level–dependent potential of BMSCs for the next 14-day differentiation regardless of the O_2 variation situations, such as development, damage, regeneration, and pathogenesis in bones. The media served an environmentally inductive role for bone regeneration, as seen in vivo so that the effect of the area-dependent O_2 level on osteogenic differentiation of BMSC could be confirmed. The high-O_2 area promoted the expression of osteogenic markers [RUNX2, COL1, and Osteocalcin (OCN)] and protein levels (RUNX2 and COL1) (Fig. 5, A and B). The results were confirmed through the increased alkaline phosphatase (ALP) activity and intracellular calcium level in the high-O_2 area compared to the low- and middle-O_2 area (figs. S10 and S11). Even BMSCs at the low-O_2 area increased expression of COL1, OCN, and RUNX2 significantly from days 7 to 14. The results indicate that the osteogenic action might be suppressed

during the early day 7 to induce chondrogenesis and then promoted through transition until day 14, as guided by the low-O_2 level in alignment with the endochondral osteogenesis mechanism.

We validated these results further using a rabbit calvaria defect model with 8 weeks of sample implantation (Fig. 5C). This model was particularly used to validate the chip result that the continuous supply of high-O_2 concentration promoted the direct osteogenesis of native BMSCs by suppressing chondrogenesis in contrast to the osteochondral defect model. Again, the use of hydrogel prevented direct contact with neighboring tissues so that diffusive O_2 effects could be maximized. After BMSCs were embedded in a fresh gelatin hydrogel without prior culture in the chip, we immediately implanted the test samples (blank, only hydrogel, and BMSC + hydrogel). First, before the defect with sample implantation, we confirmed the dense vasculature of the normal calvaria bone of mouse by microbead perfusion staining (Fig. 5D). The regeneration of high-O_2 bone in a blank area upon calvaria defects was promoted significantly by the synergistic action between BMSC and hydrogel compared to hydrogel only. We determined these results by µ-CT imaging with quantitative analysis (Fig. 5E), histological analyses [hematoxylin and eosin (H&E) and Masson's trichrome (MT) staining] (Fig. 5F), and protein expression of osteogenesis-related markers (VEGF, RUNX2, COL1, and OCN) with staining of HuNu (Fig. 5G). These results suggest that the hydrogel serves as a scaffolding role to fill the gap so that BMSCs can efficiently undergo osteogenic differentiation likely in response to the vascularized environment with O_2 supply, as seen in the chip.

DISCUSSION
The body is one of the most efficient bioreactors for numerous cell and tissue types because it maintains site-specific O_2 levels, pH, water content, and temperature safely from the ambient environment by managing the proper gradient of each parameter. Functional harmonization of complex environmental factors in the body directs the development and regeneration of multiple organs. Because it is impossible in the body, the conceptual significance of this study lies in the chip-enabled decoupling of the O_2 roles from the synchronized effects among the environmental factors. Hence, the results support a clear translation of the supportive O_2 roles in the repair, regeneration, and restoration of the skeletal system. As O_2 represents an inevitable factor for all body processes, the chip was developed to mimic O_2 variation throughout neighboring organs in a diffusive fashion. The generation of O_2 gradient by controlling the diffusive fashion set up a punchline approach to monitoring MSC responses to the relative variations of O_2 concentration within the defined space. The diffusive nature of chondrogenic and osteogenic cell response to the O_2 gradient is validated by simultaneously probing the area and time-dependent migration of chondrocyte and osteoblast toward the low- and high-O_2 areas, respectively (fig. S6). This result plays a key role in supporting each area (high, middle, and low O_2 level)–specified interpretation of MSC responses in the chip. The aligned results among the computational modeling, in vitro ruthenium signals, and in vivo sensor measurement justify the definition of the three areas. This approach is impactful because cells can sense gradient changes of each environmental parameter (*27*, *28*), thereby taking actions to deal with either abnormal or normal variations of the parameter. Together, the concepts of decoupling and gradient in the chip

Fig. 5. Osteogenesis of BMSCs in a high-oxygen environment. (**A** and **B**) We treated BMSCs with osteogenic induction media after culturing in an O_2 variant chip for 3 days and then determined their osteogenesis according to oxygen levels in vitro. The high O_2–mediated osteogenesis was evidenced by (A) gene expression of osteogenic differentiation–related markers (RUNX2, COL1, and OCN) and (B) immunostaining of RUNX2 (green) and COL1 (red) on days 7 and 14 after sample implantations ($n = 3$). (**C** and **E** to **G**) We determined the osteogenesis of BMSCs in a high-oxygen environment using a rabbit calvaria defect model following (C) the experimental procedure ($n = 5$). (**D**) In a mouse, perfusion staining with microbeads confirmed the rich vasculature in the bone, thereby verifying the high O_2 level. (E) Osteogenic differentiation of BMSCs in the vascularized high-O_2 bone was determined by μ-CT images (left) of calvaria defects with quantitative analysis (right) of new bone volume after sample implantation for 8 weeks. (F) The Masson's trichrome (MT) (blue, bone) and hematoxylin and eosin (H&E) staining (yellow line, defect area for sample implantation) further supported this result with quantitative analysis (bottom) of defect length in low magnification and (G) immunostaining of osteogenic differentiation–related markers (i) VEGF, (ii) RUNX2, (iii) COL1, and (iv) OCN with staining of HuNu. Data = means ± SD. *$P < 0.05$, **$P < 0.01$, and ***$P < 0.001$ between the lined groups.
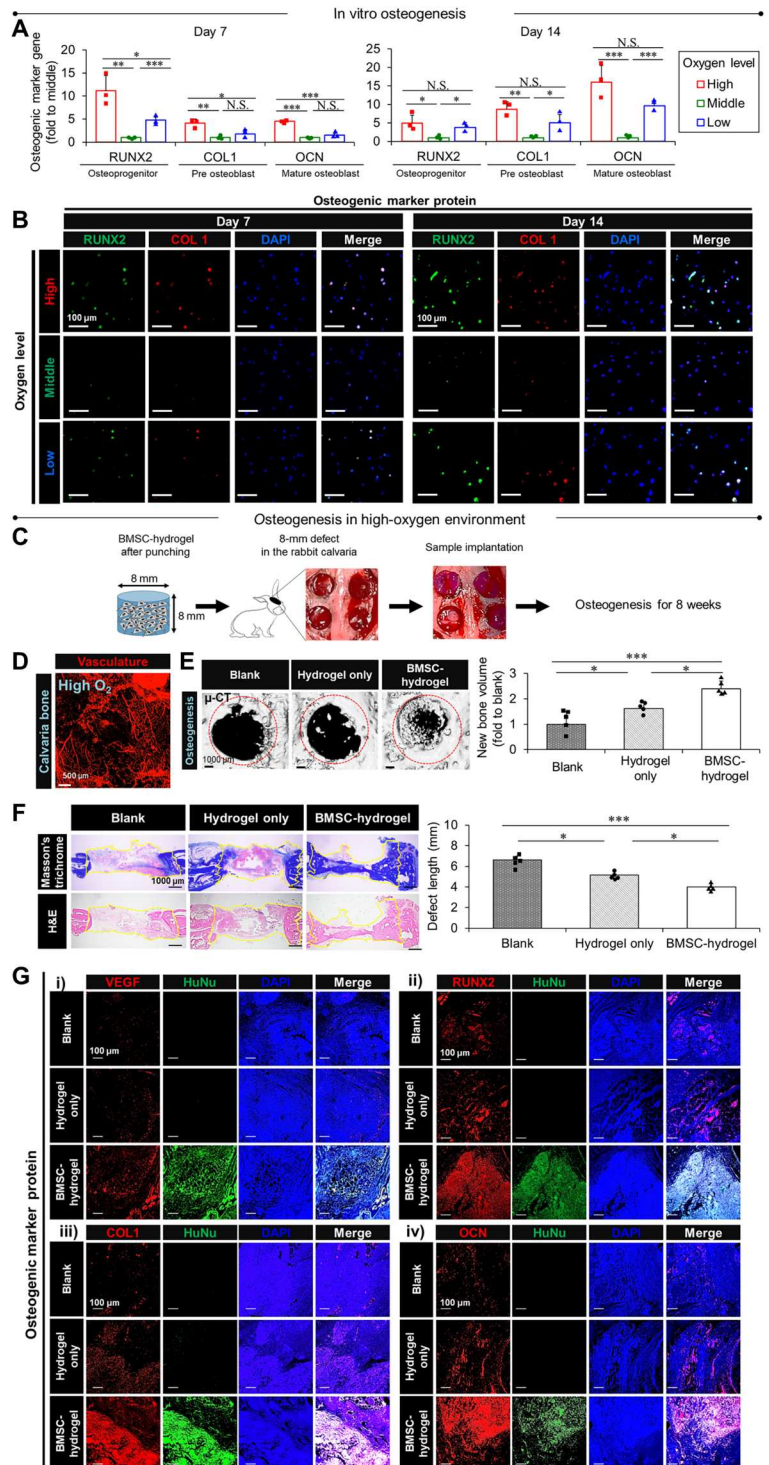
approach provided unprecedented insight into the interpretation of the supportive O_2 roles in skeletogenesis.

Moreover, the design and function of the O_2 variant chip represent breakthrough advances because (i) embedding of BMSCs into the gel enabled 3D culture as seen in the body, including the vascularized bone, vessel-free cartilage, and hypoxic bone marrow; (ii) the area-dependent variation of O_2 level resulting from the gradient

degree was controllable in a user-specified manner by modifying the rates of catalase reaction with H_2O_2 and medium perfusion; (iii) even the gel culture system provided cross-linking parameters, such as concentrations of mTG and gelatin gel, thereby enabling control of matrix stiffness so that cell migration into neighboring organs can be modulated by mimicking a normal or pathological situation; (iv) the chip design is more meaningful because the

lack of sophisticated factors allows easy use by scientists and engineers and attracts a broader readership; (v) the readout values of O_2 gradient were validated in agreement with the in vivo conditions and by computational modeling, indicating the extensibility of chip utility for clinical interpretation; and (vi) even the quiescent status of MSC in the middle O_2 indicates an unknown key to elucidate the relationships among the O_2 tension, cyclic self-renewal, and sleeping action to save the regenerative energy for the future use (46).

As justification for the experimental model, this study examined the skeletal system because the hypoxic bone marrow, vascularized bone tissue, and vessel-free cartilage are exposed to different O_2 levels. In addition, BMSCs undergo site-specific lineage transition to bone and cartilage cells by moving from the hypoxic bone marrow and by sensing environmental changes (1, 2, 39, 40). Cells can recognize relative gradient changes in the same space (27, 28). Therefore, as a routine procedure for most cell experiments, culturing cells in separate plates under different conditions and determining their activities have limitations in translating real in vivo actions. However, because each tissue condition is set up with various environmental, humoral, and matrix factors, studying the effects of each factor on the responses of corresponding tissues and cells in the body is nearly impossible. In the chip, the three different areas were divided considering the matched differences in the oxygen concentration and distance from one another ($P < 0.05$) with the results from both computational modeling and oxygen sensor measurement. The separation by the oxygen concentration and distance helped avoid sudden and sharp gradient–misled analyses under shortly apart spaces and enabled quantitative analyses with a sufficient number of cells.

In particular, processes are operated by spatiotemporal changes in these factors, representing hurdles in translating the clear effects of a single factor. For example, the transition from chondrogenic to osteogenic differentiation of BMSCs is mediated by hypertrophic phenotype changes upon exposure to incremental O_2 levels with VEGF enrichment by vascular supply from surrounding tissues (endochondral osteogenesis) (16–18). In addition, BMSCs directly undergo osteogenic differentiation in the environment where O_2 is supplied by vasculature from the skeletal system (intramembranous osteogenesis) (20). These processes also provide supportive guidelines for the regeneration of the skeletal system, but discerning differences in these processes requires a special system to isolate O_2 effects by decoupling from those of other factors.

As an evidence of the unique chip utility, the overall expression levels of proangiogenic proteins increased from the middle- to the high-O_2 area and further to the low-O_2 area (Fig. 2E). The middle-O_2 area set the quiescence status of BMSCs, resulting in the faintest signature of proangiogenic protein expression. The expression trends of low- and high-O_2 areas indicate the developmental variations of MSC characteristics, including (i) the high stemness status ("birthplace" effect), (ii) the matrix remodeling stage to set up skeletogenesis, and (iii) the vascularized bone formation based on the support of process likeEC-to-MSC transition with the consequent formation of new blood vessels (31–33). First, as an indication of stemness maintenance, the proteins representing the early angiogenic potential were expressed most distinctively in the low-O_2 area compared to the other areas. In particular, most expression of GM-CSF in the low-O_2 area represents the potential to promote hematopoiesis in the bone marrow (29) and to trigger a

chondrogenic foundation (30) in addition to angiogenic stimulation. The expression of GM-CSF was attenuated in the high-O_2 area despite the maintenance of proangiogenic potential for the formation of the vascularized bone.

Next, the signature of ECM remodeling was seen in both low- and high-O_2 areas for chondrogenesis and osteogenesis, respectively, as evidenced by the expression of MMPs. The high-O_2 area promoted the expression of MMP1 over that of MMP9, indicating the promotion of bone formation by suppressing abnormal development (38, 47). A similar pattern was seen in the low-O_2 area as evidence of suppressing hypertrophic chondrogenesis (38). Last, while the process like EC-to-MSC transition supported the appearance of angiogenic signatures in both areas (31–33), the relatively more expression of TNF-α in the high-O_2 area indicates the supportive roles in MSC proliferation and osteogenic differentiation (34–38).

Hence, this study provided punchline values to decouple the O_2 role exclusively from the other factors using 3D chip technology with confirmation of the generally accepted animal models. These results suggest an unprecedented solution to interpret the functions of hypoxic bone marrow to guide the sequential (re)generation from vessel-free cartilage to vascularized bone by directing BMSC differentiation by varying the O_2 level as a key regulator. As a result, the O_2 variant chip represents a technical innovation that matches different oxygenation patterns of the skeletal system. We programmed the gradient diffusion of O_2 in the chip design because cells are more sensitive to gradient changes in the same space rather than to absolute-level changes in separate environments. This approach effectively compared the cell responses to the three O_2 levels to be validated by two common in vivo models. Hence, the animal models should be generally accepted to establish interpretational reliability in conjunction with the results from the chip and computational modeling. The interpretation of in vivo results was thus focused on the supportive roles of O_2 variation depending on the presence and absence of vasculature and the distance from adjacent vessels. This point represents a different angle of view from the previous studies that used the common in vivo models.

The needle probe of the oxygen sensor was too short to reach into the bone marrow of the rabbit. Therefore, the rat bone was used to determine the O_2 levels of three parts, which were validated in agreement with the generally accepted levels in the human body (5 to 10% in the vascularized bone, 2 to 7% in the hypoxic bone marrow, and 1 to 5% in the nonvascularized cartilage) (1). However, the three oxygen levels of the chip (average: 46% high, 23% middle, and 7% low) (Fig. 1G) were quite higher than the rabbit and human values. As cells sense gradient changes in the same space, the relative changes among the three O_2 levels in the chip were hypothesized to set the three in vivo–like conditions under a gradient fashion. The chip results were produced using human BMSCs, and the in vitro differentiation patterns were matched with those of the osteochondral defect in the rabbit model. The mouse osteoblasts (MC3T3) also migrated toward the high-O_2 area as opposed to human chondrocytes in the time-dependent gradient fashion during the 72-hour chip culture. Furthermore, there is no difference in the mechanism of osteogenesis and chondrogenesis even in different animals (48, 49). Therefore, no apparent issue appears to exist in using the O_2 levels of both chip and rat as references to interpret the human system. The three O_2 levels were aligned among the real in vivo, CFD modeling, and microsensor measurements, indicating a unique setup to process the entire

study. This was possible because we cooperatively tuned and optimized the essential factors—including mTG/gelatin gel, catalase, and H_2O_2—to support the actions of BMSCs within the 3D culture environment.

Further studies are required to identify the effects of middle O_2 level on quiescent BMSC behavior. The low-O_2 area served as a preservation place for innate BMSC phenotypes but promoted chondrogenic differentiation upon exposure to induction by chondrogenic culture media in alignment with the hypoxic bone marrow and nonvascularized area in the femur defect model, respectively. The high-O_2 area disturbed the redox balance and proliferation control and directly promoted osteogenic differentiation upon exposure to osteogenic culture media, similar to osteogenesis in the vascularized area of the femur defect and direct bone regeneration of calvaria defects. However, the middle O_2 turned off the cell cycle progression of BMSCs, which might provide a resting period for regenerative differentiation upon skeletal defects. This BMSC behavior in the middle-O_2 area could serve as a decision point to guide chondrogenesis to osteogenesis. The mismatched results of the middle-O_2 area between the chip and in vivo models require further studies on other inductive and conductive factors from the onsite environments, as seen in the physiological system.

The whole space of osteochondral or calvaria defect was used to elucidate the relationship of O_2 tension with the regeneration of three parts (i.e., vascularized bone, vessel-free cartilage, and hypoxic bone marrow). The osteochondral defect served as a 3D space model to identify the chondrogenesis to osteogenesis following the O_2 gradient as the area became closer to the vasculature in the distance. The direct conversion from the high stemness status to the high O_2 level–supported osteogenesis was studied in the calvaria defect model in the absence of the bone marrow and vessel-free cartilage. Although the O_2 could not be decoupled completely from the other environmental factors in the two in vivo models, these two models suggested the causative role of O_2 tension in the regeneration by BMSCs with the support of a hydrogel scaffold.

Further research can be carried out by upgrading the chip to elucidate the causative roles of the O_2 variation in skeletal diseases, such as osteoporosis and arthritis, thereby suggesting O_2-associated therapeutic concepts. In addition, because the functional operation of the heart, lung, brain, and liver [e.g., nonalcoholic steatohepatitis (NASH)] is closely related to the oxygen gradient (50–52), it is possible to determine the characteristic change of corresponding cells according to the oxygen gradient of the chip. Along the same line, experimental modeling of cancer, tissue necrosis, ischemia-reperfusion injury, hypertension, inflammatory response, and fibrosis is feasible by modifying the O_2 variant chip to discern the therapeutic effect in association with abnormal changes of the oxygen concentration.

METHODS
Cells and animals
Human BMSCs and human chondrocytes were purchased from Lonza (Basel, Switzerland) with no ethical issue. Mouse osteoblast (MC3T3) was obtained from American Type Culture Collection (VA, USA). We cultured these BMSCs, chondrocytes, and MC3T3s on the tissue culture plates (SPL Life Sciences, Gyeonggi-do, Republic of Korea) in Dulbecco's modified Eagle's medium, low glucose (DMEM; Gibco, Carlsbad, CA, USA),

DMEM/nutrient mixture F-12 (Gibco), and modification of minimum essential medium α, respectively, supplemented with 10% fetal bovine serum (FBS; Gibco) and 1% penicillin-streptomycin (PS; Gibco). We propagated each cell type until they reached 80% confluence and then passaged them by detachment with 0.25% trypsin/EDTA (Gibco).

We purchased Sprague-Dawley rats (8 weeks old, male) and BALB/c mice (6 weeks old, male) from Orient Inc. (Gyeonggi-do, Republic of Korea). We bought New Zealand white rabbits (2-kg male) from Doo Yeol Biotech (Seoul, Republic of Korea). The Institutional Animal Care and Use Committee of the Yonsei Laboratory Animal Research Center (permit nos. 2019-0205, 2020-0070, and 2020-0071) approved all animal protocols.

O_2 level measurement in rat bone
We anesthetized Sprague-Dawley rats by subcutaneous injection of Zoletil (30 mg/kg; Virbac, Seoul, Republic of Korea) and maintained them by isoflurane inhalation (Hana Pharm, Gyeonggi, Republic of Korea) in a continuous tube supply. We measured the O_2 levels in the cartilage, bone, and marrow of the iliac bone using a commercial needle-type oxygen microsensor (Presens, Regensburg, Germany) and by passing a 14-gauge transplant needle (JEUNG DO Bio & Plant, Seoul, Republic of Korea) through the bone.

Fabrication of O_2 variant chip
A PDMS (Dow Corning, Midland, MI, USA) mold was custom-built—2 cm (W) by 2 cm (D) by 5 mm (H)—to contain two parallel capillary tubes (diameter, 1 mm; intertube gap, 13 mm) through casting, curing, and surfacing modification to adhere to a glass plate. During the process, we removed the tubes before curing and then inserted 19-gauge blunt-end needles with luers (Cole-Parmer, Vernon Hills, IL, USA) connected to silicone tubes (inside diameter, 0.8 mm; outer diameter, 2.4 mm; Beaverton, OR, USA) instead for medium perfusion. A gelatin/mTG solution (9:1 ratio, final concentration = 5%, w/v; hydrogel) was poured and cross-linked at 37°C for 30 min in the mold. We perfused each channel using a peristaltic pump (Longer Precision Pump Co. Ltd., Hebei, China) at a constant flow of 20 μl min^{-1} constant flow (53).

To generate O_2, we embedded catalase (Sigma-Aldrich, St. Louis, MO, USA) in an mTG gelatin gel and added H_2O_2 (Sigma-Aldrich) to DMEM supplemented with 10% FBS and 1% PS (media). We then had them react in a conical tube (SPL Life Sciences) and then perfused the media into the channel circulation using a syringe pump (KD Scientific, MA, USA) at 10 μl hour^{-1}.

O_2 generation set-up
We determined the maximum H_2O_2 concentration by assessing the viability of BMSCs (passage number = 6) after a 3-day culture in a 96-well plate (1×10^4 cells per well) under H_2O_2 treatment (0, 50, 100, 200, 400, and 800 μM) ($n = 3$) (54). We performed the Cell Counting Kit-8 (CCK-8; Dojindo, Rockville, MD, USA) assay according to the manufacturer's instructions. Briefly, we washed BMSCs with phosphate-buffered saline (PBS; Welgene, Gyeongsan, Republic of Korea) and incubated them with 10% (v/v) CCK-8 in serum-free media for 4 hours at 37°C, followed by absorbance reading at 450 nm using a colorimetric microplate reader (BioTek, Winooski, VT, USA).

We determined the gelatin concentration by checking the absence of gel flow while inverting the vials on days 1 and 3 after catalase reaction with H_2O_2 under mTG cross-linking. We mixed two different concentrations of gelatin/mTG (9:1 ratio; final concentration, 5 and 10%, w/v) with 5 mg of catalase in a 10-ml scintillation vial (Sigma-Aldrich), followed by mTG cross-linking at 37°C for 10 min. We had each hydrogel sample reacting with H_2O_2 in media (100 μM) at 37°C for 3 days.

We determined the catalase concentration by checking the degradation of the gelatin gel. We mixed a gelatin/mTG (10%, w/v) solution with catalases (0, 5, and 10 mg ml^{-1}) in a 50-ml conical tube, followed by cross-linking mTG at 37°C for 10 min. Then, we incubated each sample that was incubated with media at 37°C for 3 days, washed with PBS, and then lyophilized. We measured the dry weight ratio between days 1 and 3 as an indication of progressive gel degradation. ($n = 3$ in all experiment).

CFD modeling

We used CFD modeling of O_2 diffusion and consumption to simulate the gradient variation of O_2 levels in the gap area (1.33 cm) between the media and media + O_2 supply channels (diameter, 1 mm) of the chip: 2 cm (W) by 2 cm (D) by 5 mm (H). When the O_2 gradient in the chip was calculated by computational modeling, we considered the O_2 consumption of BMSCs along with the O_2 supply through media to set up the chip circulation system (see Supplementary Text) (55–57). Color coding from contour and volume rendering via quantitative analyses of 3D modeling showed the O_2 levels. The pressure drop is proportional to the flow velocity and inertia when a fluid with a low Reynolds number has a non-Newtonian flow property within a porous media, according to Darcy's flow law. Hence, we set the viscosity resistance and diffusion capacity of dissolved oxygen to 7.5×10^{11} m^{-2} (58) and 2×10^{-9} m^2 s^{-1}, respectively. Accordingly, we calculated the fluid movement in the chip using the ANSYS software 2020 R1 (Canonsburg, PA, USA) by meshing the 3D chip geometry to 186,417. We calculated the pressure drop in the porous media using the following formula

$$-\frac{\mu}{\kappa} \, q = \nabla p$$

Here, the medium parameters were set to the following by assuming a Newtonian fluid as a mixture of pure water and oxygen:

1) Flow rate (q) of 20 μl min^{-1}
2) Viscosity (μ) of 9.6×10^{-4} kg (m·s)$^{-1}$
3) Viscous resistance ($1/\kappa$) of 7.5×10^{11} m^{-2}

We set the boundary wall as a completely nonslip wall and set species diffusion in the upper wall to express the oxygen consumption of the cells in the media. We used the SST k–ω turbulence model to express the nonlaminar flow in the chip and used the steady-state model to predict the oxygen saturation in the equilibrium state.

Chip characterization

We simulated the area-dependent O_2% variation in the chip by progressive color diffusion from channels by perfusing safranin-O (red; Sigma-Aldrich) and crystal violet (violet; Sigma-Aldrich) in PBS into two channels separately for 72 hours. To generate O_2, we used reacting catalases with H_2O_2, which we embedded into a gelatin gel in a 50-ml conical tube with perfusion of media (10 ml) containing H_2O_2 (100 mM) using a syringe pump at a rate of 10 μl hour^{-1}, followed by the measurement of O_2 levels using a commercial needle-type oxygen microsensor (59).

We visualized and quantified chip area–dependent O_2 levels using tris (4,7-diphenyl-1,10- phenanthroline) ruthenium (II) dichloride (ruthenium; Alfa Aesar, Ward Hill, MA, USA), which quenches fluorescence signal after reaction with oxygen (26, 60). Hence, as the O_2 concentration increases, the ruthenium signal decreases by quenching the O_2. We cultured gelatin gel on the chip for 3 days, treated them with ruthenium (100 μM), and imaged them by confocal microscopy (LSM980, Zeiss, Oberkochen, Germany), followed by quantitative image analysis using ImageJ software [version 1.8, National Institutes of Health (NIH), Bethesda, MD, USA] ($n = 3$). In addition, we quantified the area-dependent O_2 levels using a commercial needle-type oxygen microsensor (59).

The three different areas were determined considering the significant differences in the oxygen concentration and distance from one another ($P < 0.05$) according to the results from both computational modeling and oxygen sensor measurement. The three areas (O_2%, distance from the left end of media + O_2) were divided by the high (20% or more, 1 to 6 mm), low (less than 10%, 8 to 14 mm), and middle (10 to 20%, 14 to 18 mm) levels so that assay results were reproducibly generated from the consistent divisions.

To determine the O_2 level–dependent cell viability, we used a LIVE/DEAD viability/cytotoxicity kit (Thermo Fisher Scientific, Waltham, MA, USA) by following the manufacturer's instructions after culture of BMSCs (1×10^6 cells/ml; passage number = 6) on the chip for 3 days. We incubated BMSCs in media containing ethidium homodimer-1 (2 mM; dead, red) and Calcein acetoxymethyl (Calcein AM, 4 mM; live, green) for 1 hour, followed by confocal imaging (LSM980, Zeiss) with quantitative image analysis using the ImageJ software (version 1.8, NIH) ($n = 5$).

O$_2$ level–gudied cell migration in the chip

After the cell reached 80% confluence, human chondrocyte and mouse osteoblast (MC3T3) were labeled with fluorescent dye [1,1'--dioctadecyl-3,3,3',3'- tetramethylindodicarbocyanine, 4-chlorobenzenesulfonate salt (DiD; red); 1,1'-dioctadecyl-3,3,3',3'-tetramethylindocarbocyanine perchlorate (DiI; orange), and 3,3'-dioctadecyloxacarbocyanine, perchlorate (DiO; green); Thermo Fisher Scientific] according to the manufacturer's instructions, followed by three washes. Next, the labeled cells were mix with hydrogel and embedded orange DiI−, green DiO−, and red DiD–labeled cells on the high-, middle-, and low-O_2 areas, respectively, in the O_2 variant chip [1×10^6 cells/ml; passage number = 3 (human chondrocyte) and 6 (MC3T3)]. The cell migration was imaged over time for 72 hour by confocal imaging (LSM980, Zeiss).

BMSC stemness in the chip

We cultured BMSCs (1×10^6 cells/ml; passage number = 6) for 3 days ($n = 3$ for each assay type). We determined the expression of stemness-related genes (SOX2, OCT4, NANOG, and GDF3) and BMSC marker genes (CD90, CD73, and CD105) by real-time quantitative reverse transcription polymerase chain reaction (real-time qRT-PCR) and the protein expression of stemness markers (SOX2 and OCT4) by immunocytochemistry. In addition, we used real-time qRT-PCR to determine marker gene expression of self-renewal in the cell cycle (CCNA, CCNB, CDK1, and CDK2)

angiogenesis (CD34, CD31, Flk1, VEGF, ANGPT1, and PDGFRβ) as supportive indications of stemness.

To confirm angiogenic gene expression at the protein level, we used the human angiogenesis array (Abcam, Cambridge, UK) following the manufacturer's instructions. We washed samples with PBS and lysed them in 1 ml of radioimmunoprecipitation assay (RIPA) buffer (Sigma-Aldrich) overnight at 4°C. The Bradford assay (Sigma-Aldrich) was used to normalize each readout value to the corresponding protein amount of chip region as an indication of cell number because BMSCs might be under a quiescence or self-renewal stage depending on the region. The supplier's blocking buffer (2 ml) was used for 30 min at room temperature (RT) to block the membrane, followed by addition of the lysate solution (500 μg of protein in 1 ml of RIPA buffer) to the membrane. The samples were then incubated for 2 hours at RT and washed three times. Then, we had the biotinylated antibody cocktail react for 2 hours at RT. We washed the samples three times and had them react with horseradish peroxidase–conjugated streptavidin for 2 hours at RT. We incubated the detection buffer mixture with the membrane for 2 min at RT and then visualized it using an LAS-3000 image analyzer (Fujifilm, Tokyo, Japan).

Because BMSCs require energy to maintain stemness, we determined ATP levels after chopping and lysing the samples in ATP assay buffer (100 μl). Using an ATP reaction mix (50 μl) at RT for 30 min caused the lysate solution (50 μl) to react, followed by absorbance reading at 570 nm in a colorimetric microplate reader. We determined ATP levels using a standard curve and normalized to the amount of the corresponding total protein obtained from the Bradford assay (Sigma-Aldrich).

Redox balance and growth control of BMSCs in the chip
To characterize the O_2 level–dependent redox balance and growth control of BMSCs, we cultured BMSCs (1×10^6 cells/ml; passage number = 6) in an O_2 variant chip for 3 days ($n = 3$ for each assay type). First, we used real-time qRT-PCR to determine the marker gene expression of hypoxia (HIF1-α), antioxidant response (GSTA2, SOD2, and TXN), proliferation (Ki67, PCNA, ERK, AKT, CCNC, CCND, CDK3, and CDK4), and anti–self-renewal (p16 and p21). Next, we used immunocytochemistry to determine the protein marker expression of proliferation (ERK and AKT).

To assess the antioxidant capacity of BMSCs, we used an assay kit (Sigma-Aldrich), which provided all buffers and reagents. We chopped samples in a lysis buffer; each lysate solution (10 μl) reacted with 2,2'-azino-bis(3-ethylbenzothiazoline-6-sulfonic acid) (ABST) substrate solution (150 μl) and myoglobin solution (20 μl) for 5 min at RT, followed by the addition of a stop solution (100 μl). We used a colorimetric microplate reader to read absorbance at 405 nm and then used the Bradford assay (Sigma-Aldrich) to normalize the corresponding total protein.

To indicate oxidative stress, we determined the intracellular NADH/NAD$^+$ ratio using a colorimetric kit (BioVision, CA, USA) with reagents and buffers following the manufacturer's instructions. We chopped each sample into the lysis buffer and heated half of the lysate solution at 60°C for 30 min to decompose NAD$^+$ to NAD, while leaving NADH intact. To cause the sample to react, we use the NAD-cycling enzyme, followed by absorbance reading at 450 nm in a colorimetric microplate reader. We used the other half of the lysate solution to quantify the amount of NADH with a standard curve and then calculated the NADH/

NAD$^+$ ratio. We used the Bradford assay (Sigma-Aldrich) to normalize each absorbance to that of the corresponding total protein.

To determine the intracellular oxidative stress level, we incubated MitoTracker Red CM-H2Xros selective probe (Thermo Fisher Scientific) with each sample for 1 hour. We stained cell nuclei and cytoskeleton using Hoechst 33342 (1:200; Invitrogen, Waltham, MA, USA) and Alexa Fluor 488 phalloidin (1:200; Invitrogen), respectively, followed by confocal imaging (LSM980).

BMSC differentiation in the chip
To determine the O_2 level–dependent chondrogenesis and osteogenesis of BMSCs, we cultured the cells for 3 days in the chip. Then, we harvested the BMSCs from the three areas and subjected them to chondrogenic induction (Gibco) or osteogenic induction media (Science, Carlsbad, CA, USA) for 14 days under the general normoxia (20% O_2) condition. We used real-time qRT-PCR to determine marker gene expression in chondrogenesis (SOX9, aggrecan, and Col2a1) and osteogenesis (RUNX2, COL1, and OCN). We used immunocytochemistry to assess marker protein expression in chondrogenesis (aggrecan and Col2a1) and osteogenesis (RUNX2 and COL1).

To assess the content levels of GAG in BMSCs during chondrogenesis, we determined the content of GAG and DNA using a Blyscan kit (Biocolor, County Antrim, UK) and Quant-iT Pico-Green double-stranded DNA (dsDNA) assay kits (Thermo Fisher Scientific), respectively, following the manufacturer's instructions. Briefly, we chopped samples in a papain solution and heated them at 60°C for 6 hours. Each lysate solution was used in DNA and GAG assay. As an indication of cell population, the DNA content was quantified that Quant-iT PicoGreen dsDNA reacted with lysate sample for 5 min. The absorbance was read at fluorescein wavelengths (excitation: 480 nm; emission, 520 nm) using a fluorescence microplate reader (Varioskan Flash 3001, Thermo Fisher Scientific). Next, the GAG content was quantified that 1,9-dimethyl-methylene blue cationic dye binds to the sulfated GAG in lysate sample. The reaction product was centrifuged for 30 min at 14,000 rpm. After resuspension using a dye dissociation buffer, the absorbance was read at 656 nm using a colorimetric microplate reader.

To assess the ALP activity in BMSCs during osteogenesis, we determined the content of ALP and DNA (cell population) using an ALP activity colorimetric assay kit (BioVision) and Quant-iT Pico-Green dsDNA assay, respectively, following the manufacturer's instructions. Briefly, we chopped samples in an assay buffer. Each lysate solution was used in ALP and DNA assay. The ALP activity was quantified that the p-nitrophenyl phosphate (pNPP) solution reacted with the lysate solution at 25°C for 1 hour. After adding stop solution, the absorbance was read at 405 nm using a colorimetric microplate reader.

As a functional indication of osteogenesis, we determined the intracellular calcium level and the protein amount (cell population) of BMSCs using a QuantiChrom calcium assay kit (BioAssay Systems, Hayward, CA, USA) and Bradford assay, respectively, following the manufacturer's instruction. Briefly, samples were harvested and dissolved in 0.5 M hydrogen chloride (HCl; Sigma-Aldrich) solution at 60°C for overnight. Each lysate solution was used for the calcium and protein assays. The calcium was quantified in the way that phenolsulphonephthalein dye reacted with free calcium in lysate buffer

for 3 min, followed by reading the optical density at 612 nm using a colorimetric microplate reader.

Real-time qRT-PCR

After culturing in the O_2 variant chip, we extracted total RNA from the cells using TRIzol (Invitrogen) and then used a NanoDrop 2000 spectrophotometer (Thermo Fisher Scientific) to quantify. To produce cDNA, we used AccuPower CycleScript RT Premix (Bioneer, Daejeon, Republic of Korea) on a T-100 thermal cycler (Bio-Rad, CA) and subjected it to real-time qRT-PCR (StepOne Plus RT PCR System, Applied Biosystems, Waltham, MA) using a primer set (table S1), cDNA, and SYBR Green PCR mix (Applied Biosystems), followed by a melting curve analysis. We normalized each result to that of glyceraldehyde 3-phosphate dehydrogenase and analyzed each result by the comparative C_t ($2^{-\Delta\Delta C_t}$) method. We also normalized the values to those of the middle O_2 level area with the presentation of fold changes.

Immunocytochemistry

After culturing in the O_2 variant chip, we harvested cells, rinsed them three times with PBS, and fixed them with 4% paraformaldehyde (CellNest, Gyeonggi, Republic of Korea) for 30 min at RT. We permeabilized the samples with 0.3% Tween 20 (Sigma-Aldrich) in PBS for 1 hour at RT and then blocked them with 0.3% Tween 20 and 3% bovine serum albumin (Millipore, MA, USA) for 1 hour at RT. We treated the samples with primary antibodies overnight at 4°C for analysis of stemness [rabbit anti-SOX2 (1:100; Novus, CO) and mouse anti-OCT4 (1:100; Novus)], proliferation [rabbit anti-ERK (1:100; Cell Signaling Technology, MA) and rabbit anti-AKT (1:100; Cell Signaling Technology)], chondrogenesis [rabbit anti-aggrecan (1:100; Abcam) and mouse anti-Col2a1 (1:100; Millipore)], and osteogenesis [mouse anti-RUNX2 (1:100; Abcam) and mouse anti-COL1 (1:100; Millipore)]. We then washed the samples and treated them with secondary antibodies in PBS for 2 hours at RT. The secondary antibodies used included anti-mouse Alexa Fluor 488, anti-mouse Alexa Fluor 594, anti-rabbit conjugated to Alexa Fluor 488, and anti-rabbit conjugated to Alexa Fluor 594 (the Jackson Laboratory, Bar Harbor, ME, USA). We counterstained the nuclei with Hoechst 33342 (1:200), followed by confocal imaging (LSM980).

Vasculature visualization in cartilage and bone of mouse

We anesthetized each BALB/c mouse subcutaneously with Zoletil (30 mg/kg) and used isoflurane to maintain inhalation in a continuous tube. To visualize the vasculature of normal cartilage and bone without defects with sample implantation, we perfused red fluorescent microbeads into the circulation system of mouse. Briefly, we perfused heparinized PBS (10 IU/ml) via the left ventricle after cutting the internal vena cava to drain whole blood. We subsequently perfused the left ventricle with heparinized PBS containing red fluorescent microbeads (100 nm in diameter; Thermo Fisher Scientific) so we could visualize all blood vessels throughout the mice, and then we harvested the long bone and skull, as well as the confocal imaging (LSM980, Zeiss).

Chondro-to-osteogenesis by BMSCs in a defect model of rabbit femur

We anesthetized rabbits by subcutaneous injection of Zoletil (10 mg/kg) and subjected them to endotracheal inhalation of isoflurane

in a continuous tube supply. Hypodermal injection of cyclosporine (10 mg/kg; Chong Kun Dang Group, Seoul, Republic of Korea) suppressed the immune rejection in human BMSC transplantation daily until scarification.

To assess chondro-to-osteogenic differentiation of BMSCs upon transition of the low-O_2 cartilage to high-O_2 bone environment, we made a medial parapatellar incision (2 cm) in the knee ($n = 5$ rabbits) and then laterally dislocated the patella to expose the articular cartilage. We created two cylindrical defects (diameter, 3 mm; depth, 3 mm) using a motorized drill (diameter, 3 mm; Saeshin, Daegu, Republic of Korea). To avoid drilling heat-mediated denaturation of surrounding tissues, we irrigated them with saline (Daehan Pharmaceutical, Seoul, Republic of Korea) during the defecting process, which also removed tissue debris.

We encapsulated BMSCs (1×10^6 cells/ml; passage number = 6) in a fresh mTG/gelatin gel with cross-linking without prior culture in the chip. We immediately punched the gel with BMSCs without preculture using a biopsy (Miltex, NJ) to a round shape (diameter, 3 mm) and used that gel to fill the defects, while an empty defect served as a control. We closed the soft tissue and skin using 4-0 nylon suture (Ailee Co. Ltd., Seoul, Republic of Korea).

After a 4-week implantation, we euthanized the rabbits by intravenous injection of 10 mEq of KCl (Daihan Pharm, Seoul, Republic of Korea). We harvested, dissected, and fixed femurs in 10% paraformaldehyde (Biosesang, Gyeonggi, Republic of Korea) for 1 day. To examine bone regeneration in the fixed femurs, we used μ-CT (Quantum GX2 microCT imaging system, PerkinElmer, Waltham, MA, USA). We used a 3D rendering software—specifically, RadiAnt DICOM Viewer 4.2.1—to analyze the defects in the corresponding region of interest (ROI).

Next, we treated the fixed femurs with a decalcifying solution-lite (Sigma-Aldrich), embedded them in paraffin wax, and then sectioned the paraffin blocks to 4-μm-thick slices using a microtome (Leica Microsystems, Deerfield, IL, USA). We purchased all the staining reagents from Sigma-Aldrich. We subjected the slices to hydration and MT or H&E staining by following standard protocols. In addition, we subjected the hydrated paraffin sections to safranin-O staining (0.1%, w/v) for 5 min after sequential treatment with hematoxylin for 5 min, fast green (0.1%, w/v) for 3 min, and acetic acid (1%, w/v) for 5 s. We used optical microscopy (Leica DMi8, Leica Microsystems) to image all stained slides.

To determine protein marker expression of chondrogenesis in the hydrated slices with blocking, we conducted immunostaining with the overnight treatment of rabbit anti-SOX9 (1:100; Millipore), rabbit anti-Col2a1 (1:100; Abcam), or rabbit anti-aggrecan (1:100; Invitrogen) with mouse anti-HuNu (1:20; Millipore) at 4°C. We characterized hypertrophic chondrogenesis toward osteogenesis with overnight treatment of rabbit anti-MMP9 (1:100; Novus), rabbit anti-MMP13 (1:100; Abcam), and rabbit anti-ColX (1:100; Abcam) with mouse anti-HuNu (1:20; Millipore) at 4°C. We incubated the slices with the secondary antibodies, as described above, for 2 hours at RT. Then, we counterstained nuclei with Hoechst 33342 (1:200; Invitrogen), followed by confocal imaging (LSM980).

Osteogenesis by BMSCs in a defect model of rabbit calvaria

To assess osteogenesis of BMSCs in the high-O_2 bone environment, we used a calvaria defect model in rabbits after treatment with Zoletil and cyclosporine, as described in the previous section ($n = 5$ rabbits). The rabbits underwent scalp shaving using an

animal clipper (JEUNG DO Bio & Plant), midline scalp incision (2 cm) in the calvarium, copious saline irrigation, and drilling of four round-shaped defects (diameter, 8 mm) on the calvaria bone using a hollow trephine bur (Saeshin). To avoid drilling heat-mediated denaturation of the surrounding tissues, we used saline irrigation during the defect process, which also completely removed bone debris. We encapsulated BMSCs (1×10^6 cells/ml; passage number = 6) in an mTG/gelatin gel with cross-linking. We immediately punched the gel with BMSCs without preculture using a biopsy (Miltex, NJ) to a round shape (diameter, 8 mm) and then used it to fill the defects, with an empty defect serving as a control. We sutured the periosteum and skin using 4-0 Vicryl (Ethicon Inc., NJ) and 4-0 nylon suture, respectively.

After an 8-week implantation, we used intravenous injections of 10 mEq of KCl to euthanize the rabbits. We harvested and dissected each calvaria bone and fixed them in 10% paraformaldehyde for 1 day. To examine bone regeneration in the fixed calvaria, we used μ-CT (Quantum GX2 microCT imaging system, PerkinElmer). We analyzed the corresponding ROI in the defects using a 3D rendering software (RadiAnt DICOM Viewer 4.2.1).

We sectioned and stained the blocks with MT or H&E. To assess protein marker expression of osteogenesis, we stained the slices using rabbit anti-VEGF (1:100; Cell Signaling Technology), rabbit anti-RUNX2 (1:100; Abcam), rabbit anti-COL1 (1:100; Abcam), or rabbit anti-OCN (1:100; Novus) antibodies with mouse anti-HuNu (1:20; Millipore). We used a confocal microscope—specifically, LSM980—to image all the stained slides.

Statistical analysis

We performed normality testing using Shapiro-Wilk by SPSS26 (SPSS Inc., Chicago, IL, USA). We use five methods to analyze statistical comparisons: If the results of the normality test dissatisfy, then a nonparametric test was used—Mann-Witney for only two groups with one factor and Kryskall-Wallis for more than two groups with one factor by SPSS26. If the results of the normality test satisfy, then parametric test was used—t test for only two groups with one factor, one-way analysis of variance (ANOVA) for more than two groups with one factor, and two-way ANOVA with Tukey's post hoc analysis for more than two groups with more than one factor by SPSS26. P values are denoted in each figure and its legend.

Supplementary Materials

This PDF file includes:
Supplementary Text
Figs. S1 to S11
Table S1

REFERENCES AND NOTES

1. G. D'Ippolito, S. Diabira, G. A. Howard, B. A. Roos, P. C. Schiller, Low oxygen tension inhibits osteogenic differentiation and enhances stemness of human MIAMI cells. *Bone* **39**, 513–522 (2006).

2. I. Rosova, M. Dao, B. Capoccia, D. Link, J. A. Nolta, Hypoxic preconditioning results in increased motility and improved therapeutic potential of human mesenchymal stem cells. *Stem Cells* **26**, 2173–2182 (2008).

3. D. W. Wang, B. Fermor, J. M. Gimble, H. A. Awad, F. Guilak, Influence of oxygen on the proliferation and metabolism of adipose derived adult stem cells. *J. Cell. Physiol.* **204**, 184–191 (2005).

4. L. Packer, K. Fuehr, Low oxygen concentration extends the lifespan of cultured human diploid cells. *Nature* **267**, 423–425 (1977).

5. P. Malladi, Y. Xu, M. Chiou, A. J. Giaccia, M. T. Longaker, Effect of reduced oxygen tension on chondrogenesis and osteogenesis in adipose-derived mesenchymal cells. *Am. J. Physiol. Cell Physiol.* **290**, C1139–C1146 (2006).

6. S. Y. Kwon, S. Y. Chun, Y.-S. Ha, D. H. Kim, J. Kim, P. H. Song, H. T. Kim, E. S. Yoo, B. S. Kim, T. G. Kwon, Hypoxia enhances cell properties of human mesenchymal stem cells. *Tissue Eng. Regen. Med.* **14**, 595–604 (2017).

7. L. Chen, A. Endler, F. Shibasaki, Hypoxia and angiogenesis: Regulation of hypoxia-inducible factors via novel binding factors. *Exp. Mol. Med.* **41**, 849–857 (2009).

8. R. D. Guzy, B. Hoyos, E. Robin, H. Chen, L. Liu, K. D. Mansfield, M. C. Simon, U. Hammerling, P. T. Schumacker, Mitochondrial complex III is required for hypoxia-induced ROS production and cellular oxygen sensing. *Cell Metab.* **1**, 401–408 (2005).

9. T. Finkel, N. J. Holbrook, Oxidants, oxidative stress and the biology of ageing. *Nature* **408**, 239–247 (2000).

10. D. M. Bell, K. K. Leung, S. C. Wheatley, L. J. Ng, S. Zhou, K. W. Ling, M. H. Sham, P. Koopman, P. P. Tam, K. S. Cheah, SOX9 directly regulates the type-II collagen gene. *Nat. Genet.* **16**, 174–178 (1997).

11. S. Sieber, M. Michaelis, H. Guhring, S. Lindemann, A. Gigout, Importance of osmolarity and oxygen tension for cartilage tissue engineering. *Biores. Open Access* **9**, 106–115 (2020).

12. C. Domm, M. Schunke, K. Christesen, B. Kurz, Redifferentiation of dedifferentiated bovine articular chondrocytes in alginate culture under low oxygen tension. *Osteoarthr. Cartil.* **10**, 13–22 (2002).

13. A. E. van der Windt, E. Haak, R. H. J. Das, N. Kops, T. J. M. Welting, M. M. J. Caron, N. P. van Til, J. A. N. Verhaar, H. Weinans, H. Jahr, Physiological tonicity improves human chondrogenic marker expression through nuclear factor of activated T-cells 5 in vitro. *Arthritis Res. Ther.* **12**, R100 (2010).

14. C. Maes, G. Carmeliet, E. Schipani, Hypoxia-driven pathways in bone development, regeneration and disease. *Nat. Rev. Rheumatol.* **8**, 358–366 (2012).

15. Y. Hiraki, C. Shukunami, Angiogenesis inhibitors localized in hypovascular mesenchymal tissues: Chondromodulin-I and tenomodulin. *Connect. Tissue Res.* **46**, 3–11 (2005).

16. M. A. Arnold, Y. Kim, M. P. Czubryt, D. Phan, J. McAnally, X. Qi, J. M. Shelton, J. A. Richardson, R. Bassel-Duby, E. N. Olson, MEF2C transcription factor controls chondrocyte hypertrophy and bone development. *Dev. Cell* **12**, 377–389 (2007).

17. T. Saito, A. Fukai, A. Mabuchi, T. Ikeda, F. Yano, S. Ohba, N. Nishida, T. Akune, N. Yoshimura, T. Nakagawa, K. Nakamura, K. Tokunaga, U.-i. Chung, H. Kawaguchi, Transcriptional regulation of endochondral ossification by HIF-2α during skeletal growth and osteoarthritis development. *Nat. Med.* **16**, 678–686 (2010).

18. S. Yang, J. Kim, J.-H. Ryu, H. Oh, C.-H. Chun, B. J. Kim, B. H. Min, J.-S. Chun, Hypoxia-inducible factor-2α is a catabolic regulator of osteoarthritic cartilage destruction. *Nat. Med.* **16**, 687–693 (2010).

19. N. Ortega, D. J. Behonick, Z. Werb, Matrix remodeling during endochondral ossification. *Trends Cell Biol.* **14**, 86–93 (2004).

20. A. Grosso, M. G. Burger, A. Lunger, D. J. Schaefer, A. Banfi, N. Di Maggio, It takes two to tango: Coupling of angiogenesis and osteogenesis for bone regeneration. *Front. Bioeng. Biotechnol.* **5**, 68 (2017).

21. H. K. Said, J. Hijjawi, N. Roy, J. Mogford, T. Mustoe, Transdermal sustained-delivery oxygen improves epithelial healing in a rabbit ear wound model. *Arch. Surg.* **140**, 998–1004 (2005).

22. C. K. Sen, Wound healing essentials: Let there be oxygen. *Wound Repair Regen.* **17**, 1–18 (2009).

23. C. A. Bassett, I. Herrmann, Influence of oxygen concentration and mechanical factors on differentiation of connective tissues in vitro. *Nature* **190**, 460–461 (1961).

24. P. Chaudhari, Z. Ye, Y.-Y. Jang, Roles of reactive oxygen species in the fate of stem cells. *Antioxid. Redox Signal.* **20**, 1881–1890 (2014).

25. A. Valle-Prieto, P. A. Conget, Human mesenchymal stem cells efficiently manage oxidative stress. *Stem Cells Dev.* **19**, 1885–1893 (2010).

26. J. N. Demas, D. Diemente, E. W. Harris, Oxygen quenching of charge-transfer excited states of ruthenium(II) complexes. Evidence for singlet oxygen production. *J. Am. Chem. Soc.* **95**, 6864–6865 (1973).

27. J. B. Gurdon, S. Dyson, D. S. Johnston, Cells' perception of position in a concentration gradient. *Cell* **95**, 159–162 (1998).

28. B. A. Camley, W.-J. Rappel, Cell-to-cell variation sets a tissue-rheology-dependent bound on collective gradient sensing. *Proc. Natl. Acad. Sci. U.S.A.* **114**, E10074–E10082 (2017).

29. A. J. Fleetwood, A. D. Cook, J. A. Hamilton, Functions of granulocyte-macrophage colony-stimulating factor. *Crit. Rev. Immunol.* **25**, 405–428 (2005).

30. M.-D. Truong, B. H. Choi, Y. J. Kim, M. S. Kim, B.-H. Min, Granulocyte macrophage–colony stimulating factor (GM-CSF) significantly enhances articular cartilage repair potential by microfracture. *Osteoarthr. Cartil.* **25**, 1345–1352 (2017).

31. P. Y. Chen, M. A. Schwartz, M. Simons, Endothelial-to-mesenchymal transition, vascular inflammation, and atherosclerosis. *Front Cardiovasc. Med.* **7**, 53 (2020).

32. A.-A. Zimta, O. Baru, M. Badea, S. D. Buduru, I. Berindan-Neagoe, The role of angiogenesis and pro-angiogenic exosomes in regenerative dentistry. *Int. J. Mol. Sci.* **20**, 406 (2019).

33. G. Sanchez-Duffhues, A. Garcia de Vinuesa, P. Ten Dijke, Endothelial-to-mesenchymal transition in cardiovascular diseases: Developmental signaling pathways gone awry. *Dev. Dyn.* **247**, 492–508 (2018).

34. H. A. Arnett, J. Mason, M. Marino, K. Suzuki, G. K. Matsushima, J. P. Ting, TNF alpha promotes proliferation of oligodendrocyte progenitors and remyelination. *Nat. Neurosci.* **4**, 1116–1122 (2001).

35. J. A. Miettinen, R. Pietilä, R. J. Salonen, K. Ohlmeier, K. Ylitalo, H. V. Huikuri, P. Lehenkari, Tumor necrosis factor alpha promotes the expression of immunosuppressive proteins and enhances the cell growth in a human bone marrow-derived stem cell culture. *Exp. Cell Res.* **317**, 791–801 (2011).

36. B. Osta, G. Benedetti, P. Miossec, Classical and paradoxical effects of TNF-α on bone homeostasis. *Front. Immunol.* **5**, 48 (2014).

37. L. E. Sidney, G. R. Kirkham, L. D. Buttery, Comparison of osteogenic differentiation of embryonic stem cells and primary osteoblasts revealed by responses to IL-1β, TNF-α, and IFN-γ. *Stem Cells Dev.* **23**, 605–617 (2014).

38. T. H. Vu, J. M. Shipley, G. Bergers, J. E. Berger, J. A. Helms, D. Hanahan, S. D. Shapiro, R. M. Senior, Z. Werb, MMP-9/gelatinase B is a key regulator of growth plate angiogenesis and apoptosis of hypertrophic chondrocytes. *Cell* **93**, 411–422 (1998).

39. M. G. Cipolleschi, P. Dello Sbarba, M. Olivotto, The role of hypoxia in the maintenance of hematopoietic stem cells. *Blood* **82**, 2031–2037 (1993).

40. C. Mas-Bargues, J. Sanz-Ros, A. Roman-Dominguez, M. Ingles, L. Gimeno-Mallench, M. El Alami, J. Vina-Almunia, J. Gambini, J. Vina, C. Borras, Relevance of oxygen concentration in stem cell culture for regenerative medicine. *Int. J. Mol. Sci.* **20**, 1195 (2019).

41. D. L. Jones, A. J. Wagers, No place like home: Anatomy and function of the stem cell niche. *Nat. Rev. Mol. Cell Biol.* **9**, 11–21 (2008).

42. V. A. Rafalski, E. Mancini, A. Brunet, Energy metabolism and energy-sensing pathways in mammalian embryonic and adult stem cell fate. *J. Cell Sci.* **125**, 5597–5608 (2012).

43. M. M. Nava, M. T. Raimondi, R. Pietrabissa, Controlling self-renewal and differentiation of stem cells via mechanical cues. *J. Biomed. Biotechnol.* **2012**, 797410 (2012).

44. T. Hayami, N. Endo, K. Tokunaga, H. Yamagiwa, H. Hatano, M. Uchida, H. E. Takahashi, Spatiotemporal change of rat collagenase (MMP-13) mRNA expression in the development of the rat femoral neck. *J. Bone Miner. Metab.* **18**, 185–193 (2000).

45. C. M. Kielty, A. P. Kwan, D. F. Holmes, S. L. Schor, M. E. Grant, Type X collagen, a product of hypertrophic chondrocytes. *Biochem. J.* **227**, 545–554 (1985).

46. Z. An, M. Sabalic, R. F. Bloomquist, T. E. Fowler, T. Streelman, P. T. Sharpe, A quiescent cell population replenishes mesenchymal stem cells to drive accelerated growth in mouse incisors. *Nat. Commun.* **9**, 378 (2018).

47. Y. Wu, Y. Tang, X. Zhang, Z. Chu, Y. Liu, C. Tang, MMP-1 promotes osteogenic differentiation of human bone marrow mesenchymal stem cells via the JNK and ERK pathway. *Int. J. Biochem. Cell Biol.* **129**, 105880 (2020).

48. M. Kanichai, D. Ferguson, P. J. Prendergast, V. A. Campbell, Hypoxia promotes chondrogenesis in rat mesenchymal stem cells: A role for AKT and hypoxia-inducible factor (HIF)-1alpha. *J. Cell. Physiol.* **216**, 708–715 (2008).

49. K. K. Sivaraj, R. H. Adams, Blood vessel formation and function in bone. *Development* **143**, 2706–2715 (2016).

50. C. J. Siegfried, Y.-B. Shui, Intraocular oxygen and antioxidant status: New insights on the effect of vitrectomy and glaucoma pathogenesis. *Am. J. Ophthalmol.* **203**, 12–25 (2019).

51. C. Li, W. Chaung, C. Mozayan, R. Chabra, P. Wang, R. K. Narayan, A new approach for on-demand generation of various oxygen tensions for in vitro hypoxia models. *PLOS ONE* **11**, e0155921 (2016).

52. N. G. A. Willemen, S. Hassan, M. Gurian, J. Li, I. E. Allijn, S. R. Shin, J. Leijten, Oxygen-releasing biomaterials: Current challenges and future applications. *Trends Biotechnol.* **39**, 1144–1159 (2021).

53. J. B. Lee, J. S. Park, Y. M. Shin, D. H. Lee, J.-K. Yoon, D.-H. Kim, U. H. Ko, Y. Kim, S. H. Bae, H.-J. Sung, Implantable vascularized liver chip for cross-validation of disease treatment with animal model. *Adv. Funct. Mater.* **29**, 1900075 (2019).

54. H. Chen, W. He, Z. Guo, An H_2O_2-responsive nanocarrier for dual-release of platinum anticancer drugs and O_2: Controlled release and enhanced cytotoxicity against cisplatin resistant cancer cells. *Chem. Commun.* **50**, 9714–9717 (2014).

55. Z. Hruzova Martina, Hippocampal neural stem cells rapidly change their metabolic profile during neuronal differentiation in cell culture. *Matters Select* **2**, 4–5 (2016).

56. A. Krinner, M. Zscharnack, A. Bader, D. Drasdo, J. Galle, Impact of oxygen environment on mesenchymal stem cell expansion and chondrogenic differentiation. *Cell Prolif.* **42**, 471–484 (2009).

57. D. Newby, L. Marks, F. Lyall, Dissolved oxygen concentration in culture medium: Assumptions and pitfalls. *Placenta* **26**, 353–357 (2005).

58. N. Hajilary, A. Shahmohammadi, New permeability model for gel coated porous media with radial flow. *J. Appl. Fluid Mech.* **11**, 397–404 (2018).

59. D. M. Lewis, K. M. Park, V. Tang, Y. Xu, K. Pak, T. S. Eisinger-Mathason, M. C. Simon, S. Gerecht, Intratumoral oxygen gradients mediate sarcoma cell invasion. *Proc. Natl. Acad. Sci. U.S.A.* **113**, 9292–9297 (2016).

60. H.-S. Kim, Y. M. Shin, S. Chung, D. Kim, D. B. Park, S. Baek, J. Park, S. Y. Kim, D.-H. Kim, S. W. Yi, S. Lee, J. B. Lee, J.-Y. Ko, G.-I. Im, M.-L. Kang, H.-J. Sung, Cell-membrane-derived nanoparticles with Notch-1 suppressor delivery promote hypoxic cell-cell packing and inhibit angiogenesis acting as a two-edged sword. *Adv. Mater.* **33**, e2101558 (2021).